UNIVERSITÀ DEGLI STUDI DI TRIESTE

XXIX CICLO DEL DOTTORATO DI RICERCA IN

Scienza della Terra e Meccanica del Fluidi

NUMERICAL AND EXPERIMENTAL INVESTIGATION OF SUSPENDED SEDIMENT TRANSPORT IN LAB-SCALE TURBULENT OPEN CHANNEL FLOW

DOTTORANDO: **MAHMOUD JOURABIAN**

COORDINATORE: **PROF. PIERPAOLO OMARI**

SUPERVISORE DI TESI: **PROF. VINCENZO ARMENIO**

ANNO ACCADEMICO 2016/2017

Abstract

Single-phase Euler-Euler based wall-resolving LES with the dynamic Smagorinsky model is used to investigate suspended sediment transport in a turbulent open channel flow. Aspect ratio of the open channel is high. Bottom bed is smooth. For the clear water flow, streamwise and vertical turbulence intensities in experiments of Muste et al. [2005] are much bigger than those in the wall-resolving LES and DNS by Hoyas and Jimenez [2008]. Bulk velocity in the sediment-laden flow is lesser than that in the clear water flow. Friction velocity is same for both flows. While Muste et al. [2005] recorded that in the inner region, the streamwise velocity of the sediment-laden flow was higher than that of the clear water flow, wall-resolving LES shows no alteration. In the outer region, the depth-resolved streamwise velocity of the sediment-laden flow is lower than that of the clear water flow. Introduction of suspended sand particles into the turbulent open channel flow of the clear water results in the decrease of the drag force while shear stress on the channel bed is constant. To get reduction of the bulk velocity, the fast Eulerian method in the two-way coupling should be employed.
Single-phase Euler-Euler based unresolved wall-function LES with the Smagorinsky model under the equilibrium stress assumption is implemented to understand interactions between turbulence and suspended sand particles in a turbulent open channel flow. Channel bed is rough. Aspect ratio of the open channel is low. To treat erosion from the bed, the reference concentration method together with the Shields diagram is used. Results are compared against experiments of Cellino [1998]. Suspended particles engender reduction of the friction velocity, bulk velocity and roughness in contrast to the clear water flow. Streamwise velocity is decreased in the outer region while it is expedited in the super-saturated region near the channel bed. It is due to high inter-particle collisions between sediment particles which are not bounded by viscosity. In upper levels, remarkable weakening of the vertical turbulence intensity is seen. When the buoyancy term is deactivated, the sediment concentration gets high and unsatisfactory turbulence statistics are obtained. Wall shear stress on the sidewalls of narrow open channels must be considered.
Effects of lateral and bottom macro-rough boundaries on the propagation of a suspended sediment wave in a turbulent open channel flow are shown experimentally. Least decay of the normalized concentration is for the reference

case in absence of trapping zone. Least sedimentation among lateral configurations is for case $L4$ with the highest roughness aspect ratio, cavity density and medium flow discharge. Length of the inlet reach is lowest and it boosts mixing. Highest deposition of the Polyurethane particles is for case $L5$ with the lowest roughness aspect ratio and cavity density. Discharge is also low. Turbulence is most attenuated for case $L2$ with the medium flow discharge due to adequate lengths of the inlet and outlet reach. Deposition of the Polyurethane particles and turbulence in the lateral macro-rough flows depend on the cavity aspect ratio, flow discharge, roughness aspect ratio, cavity density and location of the lateral cavities. In the bottom macro-rough flows, effects of spacing between bottom macro-rough elements on the deposition and turbulence characteristics are seen. Turbulence characteristics of upstream C_1 and downstream C_2 signals are identical for reference, $B1$ and $B1.5$ cases. When spacing is 2, highest trapping and deposition take place. Most weakening of the turbulence is seen for spacing 2. When spacing is augmented from 2 to 5, the turbulence is enhanced and trapping becomes lesser. Bottom macro-rough elements change significantly flow pattern and turbulence characteristics in a specific spacing. As spacing gets larger, effects of bottom macro-roughness elements on each other reduces more.

Acknowledgements

I give glory to Almighty God for all

This thesis was fulfilled under the fund of the European Union via SEDITRANS (REA grant agreement no. 607394), an initial training network (ITN) project supported financially by the Marie Curie Actions of the EU's 7th Framework Program.

The numerical part of this PhD thesis was done in PhD school of the Earth Science and Fluid Mechanics (ESFM) at University of Trieste (UNITS) while experimental part was accomplished at Hydraulic Constructions Laboratory of the École Polytechnique Fédérale de Lausanne (EPFL).

The anther expresses thanks to his supervisor Prof. Vincenzo Armenio for opportunity to work under his guidance and help in ESFM team.

The author is thankful of availability of the supercomputer at the University of Malta to run the LES-COAST code.

Many thanks go to Prof. Anton Schleiss, Dr. Mario J. Franca, Dr. Carmelo Juez and other technicians at Hydraulic Constructions Laboratory-EPFL for supervision of experiments and providing infrastructure.

The author wishes to thank all scientific members in ESFM group, SEDITRANS network and respectable reviewers of this PhD thesis.

Finally, my deep and sincere gratitude to my parents for their continuous and unparalleled love, help and support in my life. I am grateful to my brothers, Masoud and Mahyar, for always being there for me as a real friend. They selflessly encouraged me to seek my own destiny in life.

Thank you.

Contents

List of Figures

List of Tables

Chapter 1

Introduction

Sediment transport is a mechanism that relates hydrodynamic processes to morphological changes. Suspended sediment transport (SST) refers to particles that move along a river completely supported by the flow. To keep sediment particles in the suspension mode, upward-directed forces related to the turbulence in the flow have to become powerful enough to overcome the downward gravity force acting on particles. During previous decades, many researchers working on fluvial hydraulics elucidated partially interactions between suspended sediment particles and turbulence in wall-bounded flows with flat and rough boundaries. Since these interactions are not adequately quantified, common practice is to treat suspended sediment particles and water flow as the mixed fluid.
In the numerical part of this study, the Navier-Stokes and scalar transport equations in the mixture flow model are solved iteratively using the LES-COAST code which is developed for harbor and coastal areas. The curvilinear forms of governing equations are integrated using a modified version of the finite-difference fractional-step method in a non-staggered grid. Periodic boundary condition is set for the velocity, pressure and sediment concentration in the streamwise and spanwise directions. Sediment-laden flows are Newtonian and sediment particles are noncohesive. Four-way coupling is not taken into account. All complex phenomena such as preferential accumulation, turbophoresis or clogging of sediment particles are neglected. Firstly, using the LES-COAST code, this PhD thesis aims to unravel effects of suspended sediment particles on hydrodynamics in a turbulent open channel flow with high aspect ratio and bottom smooth wall. Data of clear water and sediment-laden flows from experiments of Muste et al. [2005] are selected for comparison. Single-phase Euler-Euler based wall-resolving LES with the dynamic Smagorinsky model is used to solve the filtered Navier-Stokes equations and scalar equation for the sediment concentration. Fast Eulearian method (FEM) in the two-way coupling framework is implemented to reproduce influences of the sediment concentration on hydrodynamics of the flow. Non-cohesive sand particles with diameter of $d = 0.00023m$ are selected. To better explain interactions between turbulence

and suspended sand particles, the sediment-laden flow with highest concentration $C = 0.00162$ is chosen. It should be understood how suspended sand particles could modify the bulk velocity and shear stress on the channel bed compared to the clear water flow. Variations of the streamwise velocity in the sediment-laden flow in contrast to the clear water flow have to be explored. Secondly, influences of suspended noncohesive sand particles on the bulk velocity, friction velocity, Reynolds stress, roughness of the channel bed, streamwise and vertical velocities in a turbulent open channel flow with rough bottom wall and low aspect ratio are researched using the LES-COAST code. Single-phase Euler-Euler based unresolved wall-function LES under the equilibrium stress assumption is employed. Smagorinsky model is used to calculate SGS stresses and sediment fluxes in the mixture flow model. Results of clear water and sediment-laden flows are compared against experiments of Cellino [1998]. A constant volumetric concentration $C = 0.00077$ of sand particles with the diameter of $d = 0.000135m$ is imposed to the fully developed clear water flow to obtain statistics of the sediment-laden flow. The reference concentration method proposed by Smith and Mclean [1977] together with the Shields diagram is used to treat the erosion of sediment particles from the channel bed. Buoyancy induced by suspended sediment particles may influence hydrodynamics of flow, and hence the two-way coupling meaning introduction of modified gravity term prescribed by Dallali and Armenio [2015] in the Navier-Stokes equations of the mixture flow is taken. Wall shear stress on the sidewalls is included in the computation of imposed pressure gradient for clear water and sediment-laden flows. The same roughness as expressed in experiments is applied for clear water and sediment-laden flows. It has to be recognized whether suspended sand particles cause attenuation or enhancement of streamwise and vertical turbulence intensities comparing to the clear water flow. Importance of the buoyancy effect in the mixture flow model should be understood.

In natural rivers, morphological irregularities on banks or bed could change flow patterns and SST. To do sediment management and to promote habitat suitability, hydraulics engineers artificially add cavities and lateral embayments to lateral river banks. Sedimentation processes depend on the geometrical configuration of river banks. Laboratory works relating to hydrodynamics and morphodynamics of lateral embayments in open channel flows are rare and complicated to perform. Although some works in past were done on investigation of turbulence characteristics of turbulent open channel flows in presence of bottom macro-rough elements, little effort is dedicated to study propagation of a suspended sediment wave in these flows. Thirdly, effects of lateral and bottom macro-rough boundaries on propagation of a suspended sediment wave in a turbulent open channel flow are shown experimentally under the steady state condition. Because of imposed volumetric flow rate $Q = 0.015m^3/s$ and flow depth $h = 0.07m$, Polyurethane particles with $s = 1.16$ and $d = 0.00008m$ are suspended in a wide open channel. Two turbidimeters are in upstream and downstream parts to show temporal concentration. Sediment-laden flows are Newtonian. Results are demonstrated in terms of normalized concentration of suspended Polyurethane particles, corresponding auto-correlations and cross-

correlations. Based on Meile [2007], Maechler [2016] and Juez et al. [2017], influences of lengths of inlet and outlet reach, aspect ratio of lateral cavity flow, roughness aspect ratio, cavity density and flow discharge on flow patterns, turbulence and deposition of suspended sediment particles are investigated. For bottom macro-rough flows, as Leonardi et al. [2004] and Leonardi et al. [2007] reported, changing spacing between bottom macro-rough elements could alter flow patterns and turbulence characteristics. Influence of spacing on propagation of a suspended sediment wave is examined here. Relationships between spacing, turbulence characteristics and trapping of sediment particles in certain discharge and flow depth are stated. For example, it is shown that with which spacing turbulence is most weakened and there is highest trapping and difference between concentration signals in upstream and downstream parts.

Chapter 2

Suspended sediment transport (SST)

2.1 Definition of suspension mode

Sediment transport is a process that links hydrodynamic processes and beach morphology. Without transport of sediments, there would be no morphological change and beach.
In principal, the bed materiel load, which is found on the bed of a stream, undergoes an exchange between the bed and fluid flow. It may move as bed-load [van Rijn, 1984a] [Wu et al., 2000] or suspended load [van Rijn, 1984b]. They are categorized by Mehta [2013].
Figure (2.1) shows that the bed-load transport (BLT) consists of sediment particles that slide, roll and saltate over the channel bed. The bed-load transport is mainly governed by the water drag and collisions among bed material. Turbulence takes an auxiliary role in maintaining saltation . When upward-directed

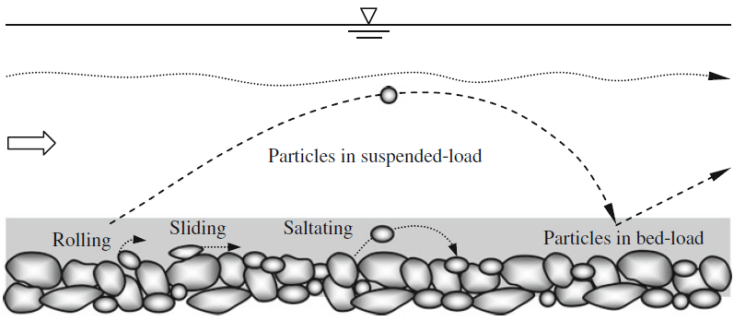

Figure 2.1 – Multifarious modes of the sediment transport taken from [Dey, 2014]

forces, which are associated with the turbulence in the flow, are strong enough to exceed significantly the downward gravity force, particles are kept in the suspension mode. Dey [2014] clarified that the suspension occurs when the ratio between the settling velocity and shear velocity becomes lower than 0.6.
SST is a prevailing process in lower reaches of rivers. Particles are also fine. Sediment concentration reduces as the vertical distance from the channel bed increases. If the turbulence intensity is diminished and the flow expands, sediment particles return to the bed.

2.2 Settling velocity

Sediment particles become suspended in the flow when the gravity force, which enforce them to fall towards bed, is surpassed by upwardly lifting forces generated by the turbulence. Particles denser than water such as sands inevitably fall in a laminar flow since the gravity force is not opposed. As gravity force becomes comparable to forces counteracting downward movement, a balance may occur. Particles are characterized with their settling velocity.
The settling velocity w_s is of prime importance in modeling of SST. When the diameter of a suspended particle moving in a fluid is in the range $0.1mm < d < 1mm$, equation (2.1) is used based on [van Rijn, 1984b] [Lin and Falconer, 1997] [Dallali and Armenio, 2015]. There is a balance between the gravity force and drag resistance,

$$w_s = \frac{10\nu}{d}\left[\left(1 + \frac{0.01\,(s-1)\,gd^3}{\nu^2}\right)^{0.5} - 1\right] \tag{2.1}$$

$$s = \frac{\rho_s}{\rho_0} \tag{2.2}$$

s is the specific gravity of suspended particles. g is the gravitational acceleration. ρ_s and ρ_0 are densities of sediment particles and water, respectively. For particles with $d < 0.1mm$, the settling velocity is estimated based on the Stokes drag law [Cheng et al., 2015],

$$w_s = \frac{1}{18}\frac{(s-1)\,gd^2}{\nu} \tag{2.3}$$

There are many factors affecting tunable settling velocity. For instance, Kawanisi and Shiozaki [2008] experimentally found out that the turbulence intensity and Stokes number St may influence mean settling velocity,

$$St = \frac{\tau_p}{\tau_\lambda} \tag{2.4}$$

τ_p and τ_λ are Stokes the response time and Taylor time scale [Elghobashi, 1994], respectively,

$$\tau_p = \frac{w_s}{g}, \tau_\lambda = \left(\frac{15\nu}{\epsilon}\right)^{\frac{1}{2}} = \frac{\lambda}{u_{rms}} \tag{2.5}$$

For a fully developed turbulent open channel flow, most energetic eddies are the Taylor scales. They are not largest (integral scales) or smallest ones (Kolmogorov scales). Dissipation takes place in the Kolmogorov scales. ϵ is the energy dissipation. It is assessed from the energy spectrum by utilizing the inertial subrange. For open channel flows, it is calculated from [Nezu and Nakagawa, 1993],

$$\frac{\epsilon h}{u_*^3} = 9.8 \left(\frac{y}{h}\right)^{-0.5} e^{\left(\frac{-3y}{h}\right)} \tag{2.6}$$

h is the water depth in open channel flows. The Taylor time scale is the characteristic timescale of the flow. λ is the Taylor length scale [Tennekes and Lumley, 1972] and u_{rms} is the root-mean-square (RMS) of the streamwise turbulent velocity fluctuation. Kawanisi and Shiozaki [2008] concluded that the settling velocity was abated by 40 percent in a flow with weak turbulence. Settling velocity was enhanced substantially in a highly turbulent flow.
Additionally, the influence of the concentration on the settling velocity was reported by Cheng [1997]. Lewis et al. [1949] used this formulation,

$$\frac{w_m}{w_s} = (1 - C)^m \tag{2.7}$$

While w_s is the settling velocity of a solitary particle in a fluid, w_m is the settling velocity of particles with the concentration C. The exponent m depends on the effective density, particle Reynolds number and volumetric concentration of the mixture.
The settling velocity depends on the inverse of the kinematic viscosity in the Stokes law. Hence, doubling the kinematic viscosity would halve the settling velocity. If fine sediments are in suspension, the viscosity of the sediment-laden flow may be higher than that of the clear water. Since the sediment concentration is highest close to the river bed, falling sediment particles may experience augmentation of the viscosity and their settling velocity may be abated.

2.3 SST in turbulent open channel flow

There are many theoretical, numerical and experimental works in the literature that focused on understanding of interactions between suspended sediment particles and turbulence in open channel flows. Simulation of the SST in the presence of macro-rough boundaries is more complicated.
Wang and Qian [1989] experimentally compared turbulence characteristics of a Newtonian flow with noncohesive particles to those of the clear water flow in a recirculating tilting flume with hydraulic smooth surface. It was mentioned that the channel roughness could affect results in the vicinity of boundary even for the clear water flow. For both plastic particle-laden flows with $s = 1.052, d = 0.000266m$ and sand-laden flows with $s = 2.64, d = 0.00015m$, the streamwise turbulence intensity was decreased with the enhancement of the

concentration. Close to the bed region $y/h < 0.2$, streamwise turbulence intensities for plastic particle-laden flows and sand-laden flows were deviated mostly from that for the clear water flow. In upper flow regions $y/h > 0.2$, the difference between the clear water flow and plastic particle-laden flows was very low. Streamwise turbulence intensity for sand-laden flows was reduced obviously with the increase of he tconcentration. Reduction of the turbulence intensity in sand-laden flows was explained by the effect of the density gradient. Particle delay played important role in damping of the turbulence near the bed in plastic particle-laden flows. Maximum of the streamwise turbulence intensity for the clear water flow with $h = 0.1m, u_* = 0.0775m/s$ was 2.3 in $y/h = 0.0535$. Autocorrelations revealed that sizes of the longitudinal eddy in sediment-laden flows were bigger than those in the clear water flow. Using the discriminator laser-Doppler velocimeter (DLDV), Muste and Patel [1997] measured the mean velocity and turbulence characteristics in open channel flows. Suspended sand particles were in the range of $0.21 - 0.25mm$. Particle velocity lagged the water velocity and it was dependent on the concentration. A small decline in streamwise particle velocity fluctuations was seen. Considerable lessening and modification of the shape of vertical velocity fluctuations were reported.
Cellino [1998] and Graf and Cellino [2002] investigated experimentally the turbulence and concentration characteristics of suspension flows in open channels. Flows were steady and uniform at the capacity condition. Sizes of sediment particles were $d = 0.000135, 0.00023$ and the concentration was small. Clear water formulation was used. Stratification effect induced by suspended particles affected the longitudinal mean velocity profile in the outer region of the flow. Largest vertical velocities, which were seen close to the free surface, were directed towards the bed. They were created by secondary currents. Suspended particles engendered slight increase of the longitudinal turbulence intensity and 40 percent suppression of the vertical turbulence intensity. There was no effect on the linear trend of the Reynolds stress.
Winterwerp [2001] employed one-dimensional (1D) k-ϵ numerical modeling to study stratification effects generated by interactions between suspension of fine-grained sediment and turbulence. Sediment-induced buoyancy effects resulted in significant interactions between suspended sediment particles and turbulence. Winterwerp [2001] also validated experiments of Coleman [1981]. Both decrease in effective von Karman constant and alteration of the velocity defect law were due to sediment-induced buoyancy effects. These results were also seen at low concentration $C = 0.001$. Guo and Julien [2001] investigated theoretically effects of the sediment suspension on governing equations and turbulence characteristics. Boussinesq approximation in stratified flows was included. Effects of the sediment concentration on the fluid density were neglected in continuity and momentum equations except the gravity term. Viscosity was constant. Velocity profiles in sediment-laden flows were analogous to those in the clear water. Modified log-wake law was valid for sediment-laden flows. Sediment suspension augmented the mean flow energy loss and abated the vertical turbulence intensity. Both average concentration and density gradient (Richardson number) diminished the von Karman constant in sediment-laden flows.

Righetti and Romano [2004] used the phase Doppler anemometry (PDA) to detect the role of solid particles on the velocity profile in the near-wall turbulence with $13000 < Re < 14500$. Fluid and particle velocities were simultaneously measured and compared to the clear water flow. Glass particles with $s = 2.6$, diameters of $100-200\times10^{-6}m$ and mean volumetric concentration of 10^{-3} were used. For sediment-laden flows, the mean velocity in the logarithmic and outer regions considerably was diminished. It was enlarged inside the inner region $y^+ < 5$. RMS fluctuations of the vertical velocity were damped in the outer region but were escalated within the inner region in contrast to the clear water flow. Close to the wall, there was increase of the Reynolds stress. Far from the wall there was a decrease.

Nezu and Azuma [2004] conducted simultaneous measurements of particles and water in particle-laden open channel flows using the discriminator particle-tracking velocimetry (PTV). Friction velocity in the sediment-laden flow was computed from the Reynolds stress. Normalized fluid velocity in the sediment-laden flow was described by the log law inside the inner wall region. Though, the von Karman constant was lessened slightly with the increment of the concentration. Average particle velocity was slightly lesser than the fluid velocity far from wall. On the other hand, the average particle velocity was bigger than the fluid velocity. These differences caused fluid-particle interactions. Turbulence intensities were almost not changed by particles far from wall, irrespective of the particle diameter and specific density. Conversely, turbulence intensities of the fluid were escalated remarkably by particles inside the wall region. Turbulence intensities of particles got bigger than those of the fluid inside the wall region. Vertical movements of particles were more increased due to ejections and sweeps.

Muste et al. [2005] and Muste et al. [2009] employed simultaneous PIV-PTV measurements to determine interactions between suspended particles and turbulent structures inside the flow. Bulk velocity in sediment-laden flows was abridged with the sediment concentration irrespective of the particle density. Suspensions of the natural sand and crushed Nylon particles extracted energy from the flow. Also, the von Karman constant gradually was decreased with the addition of particles. There was a strong particle flow turbulence within the inner region. Mean streamwise velocity of the sand particles lagged those of water flow inside the outer region. Mean streamwise velocities of particles were bigger than those of water close to the channel bed because particle velocities were not directly influenced by the no-slip condition. Vertical velocities of the sand particles were higher than those of water. Traditional mixed-flow treatment of sediment-laden flows showed inconsistencies with regard to actual flow of water and transport of suspended particles in sediment-laden flows.

Noguchi and Nezu [2009] examined the turbulence modulation in suspended sediment-laden open-channel flows. They used the discriminator particle tracking velocimetry (D-PTV) for sediment particles and the discriminator particle image velocimetry (D-PIV) for fluid tracers. It was concluded that inside region $y^+ < 15$, the particle velocity was faster than carrier fluid whereas for $y^+ > 15$, fluid became faster than particles. This relative velocity was aggrandized for

bigger particles. Pittaluga [2011] developed analytic approach to account for stratification effects on distributions of the vertical velocity and sediment concentration in fluvial channels. For a given shear stress, stratification effects induced enhanced velocity gradient and augmented streamwise velocity. Stratification caused a decrease in the suspended sediment concentration relative to the neutral condition. Increase of the sediment concentration caused enlargement of the depth-averaged velocity through stratification. It also resulted in increase of the effective bed roughness, friction and abated flow velocity.
Zhu et al. [2013] applied the modified coherent dynamic eddy model of the LES. Pick-up function was employed to simulate erosion and deposition of non-cohesive sediment particles in turbulent channel flow with high concentration. The rough wall model was used instead of high-cost LES with near-wall resolution. In the streamwise direction, sediment particles were picked up predominantly due to excess bottom stress, whereas in the spanwise direction, the turbulent mixing engendered by streamwise vortexes contributed more to the erosion. Kundu and Ghoshal [2014] developed mathematical modeling for steady uniform turbulent open channel flow laden with sediments. They incorporated effects of stratification and secondary flows. Direction and strength of secondary currents generated various mean vertical velocities and sediment concentration patterns. Stratification caused a decrease in the sediment concentration relative to the neutral case. The concentration was boosted in the flow with upward vertical velocity. It was diminished with downward vertical velocity. Yu et al. [2014] concluded that if sediment particles were in a turbulent flow over a smooth bed, the von Karman constant was reduced. Sediment particles engendered a velocity lag inside the outer region and velocity increment within the inner region. Slope of the velocity distribution was increased.
Maechler [2016] experimentally highlighted interactions between discharge, capacity concentration and aspect ratio of lateral macro-rough cavities in turbulent open channel flows. Turbulent eddies were induced by interface with calm zone and main flow. Bigger aspect ratio limited cavity sedimentation through turbulent and oscillating processes. With highest discharge, sedimentation was countered by turbulence and flow oscillations inside cavity flows.
Juez et al. [2017] carried out systematic laboratory tests in turbulent open channel flow with multifarious geometries of lateral macro-rough cavities. Idealized artificial lateral macro-roughness elements perturbed flow. The sediments remained within the cavity flow, where turbulence levels were lower than in main channel. Probability of settling was higher. As roughness was increased in lateral macro-rough flows, turbulence was enhanced and particles were more kept in the suspension mode. Settling was hindered. Decay of the sediment concentration was quicker for lower discharges. Larger discharges boosted turbulence levels and augmented sediment suspension.
Laboratory works relating to hydrodynamics and morphodynamics of lateral embayments in open channel flows are rare and complicated to perform. Moreover, few works in the literature explored interactions between suspended fine particles and turbulence in open channel flows with bottom macro-rough boundaries.

2.4 Couplings

Elghobashi [1994] classified turbulent sediment-laden flows (SLF) according to interactions between sediment particles and turbulence. There are one-way coupling ($C < 10^{-6}$), two-way coupling ($10^{-6} < C < 10^{-3}$) and four-way coupling ($C > 10^{-3}$). This classification depends on the amount of suspension load.

2.4.1 One-way coupling

The interaction is called one-way coupling [Zedler and Street, 2001] [Zedler and Street, 2006] when the volumetric concentration is lower than 10^{-6}. Dispersion of particles is dependent on the state of the turbulence and no term is introduced in the Navier-Stokes equations. Just settling velocity is appeared in the concentration equation.

2.4.2 Two-way coupling

As the volumetric concentration increases $10^{-6} < C < 10^{-3}$, the two-way coupling [Ferry and Balachandar, 2001] happens and sediment particles may transfer momentum to the flow. It engenders alteration of turbulence characteristics. It should be reminded that flows in already expressed criteria are called dilute suspensions. Abating size of particles augments the surface area of the sediment phase and dissipation rate of the turbulence energy. On the other hand, enlarging the particle response time with the particle Reynolds number in the range $Re_p > 400$ results in the vortex shedding and enhanced production of the turbulence energy. More numerical discussions on the role of the size of suspended particles in modulating turbulence could be seen in Cao et al. [2003]. Two-way coupling or interactions between base fluid and sediment particles could be imposed by introducing a modified gravity term (2.25) in the NS equation (2.22).

2.4.3 Four-way coupling

In the four-way coupling framework [Breuer and Alletto, 2012], the volumetric concentration goes beyond 0.001 and flow is a dense matter. In addition to the two-way coupling, collisions between particles are also examined. Breuer and Alletto [2012] carried out a LES-based comparison between various couplings and found out that there was a satisfactory agreement between two-way and four-way coupled simulations and experimental measurements. Because here we just focus on dilute suspensions, the four-way coupling is neglected.

2.5 Fast Eulerian method (FEM)

Numerical models for treating two-phase sediment transport are grouped as Euler-Lagrange [Soldati and Marchioli, 2012] and Euler-Euler [Chou and Fringer, 2008] [Harris and Grilli, 2014].
The Euler-Lagrangian model can be used when the concentration of particles is low. Motion of individual particles is tracked. The water is treated as a continuum. Tracking a large number of particles is very expensive from a computational point of view and it may be impractical for fine sediment suspensions. In the Euler-Euler-based models, which are more suitable for engineering applications, governing equations for both particulate and fluid phases are based on the continuum approximation. The particles follow the fluid motion except for their settling velocity which appears in the concentration equation.
Euler-Euler-based models are divided to two-phase models [Cheng and Hsu, 2014] [Chiodi et al., 2014] or single-phase models [Chou and Fringer, 2008] [Harris and Grilli, 2014] [Dallali and Armenio, 2015].
In the two-phase models, mass and momentum conservation equations for both phases are computed. Phases are differentiated by a particle volume fraction. As stated by Chiodi et al. [2014], forces, which are induced in the flow such as viscous drag, inertia, contact force, solid friction and lubrication, or Archimedes effect, could be investigated in the computation.
The single-phase or mixture model is adopted for fine particles in the suspension mode. In the mixture model, the vertical velocity is simply the sediment particle settling velocity. One advection-diffusion equation is defined for the sediment concentration in the mixture.
More specifically, Ferry and Balachandar [2001] developed the fast Eulerian method (FEM) in the two-way coupling framework to simulate the sediment-laden flow as a two-phase flow. The particle response time should be low enough compared to the characteristic time-scale of the turbulent flow. If particles are very small, they may move with the fluid and are spatially well mixed. The flow is treated as a single-phase medium with a modified density. Suppose that the Eulerian fluid and particle velocities are represented, respectively, by $u_f(\mathbf{x},t)$ and $v_p(\mathbf{x},t)$. Maxey [1987] and Druzhinin [1995] considered following Lagrangian equation (2.8) for the particle motion,

$$\frac{dv_p}{dt} = \frac{1}{\tau_p}(u_f - v_p) + g \tag{2.8}$$

The particles are subjected to only viscous drag and gravity force g. τ_p is the particle time-scale which can be obtained from Ferry and Balachandar [2001]. When expanding equation (2.8) in terms of $u_f(\mathbf{x},t)$ and $v_p(\mathbf{x},t)$, following formulation could be gained,

$$v_p = u_f - \psi\tau_p + \left(\frac{\mathbf{D}\psi}{\mathbf{D}t} + \psi.\nabla u_f\right)\tau_p^2 \tag{2.9}$$

Higher orders of the approximation are disregarded. No influence of surrounding particles on the velocity of a particle is assumed. The total derivative is defined

only for fluid elements. ψ is the modified acceleration taken as,

$$\psi = \frac{\mathbf{D}u_f}{\mathbf{D}t} - g \tag{2.10}$$

Maxey [1987] stated that the first-order version of equation (2.9) could explain the preferential accumulation of particles in regions of low vorticity and high strain. When additional forces like added-mass, Basset and Saffman lift are included in this expansion, following form could be acquired after some simplifications [Ferry and Balachandar, 2001],

$$v_p = u_f + (1-\eta)\left(-\psi\tau_p + \left(\frac{\mathbf{D}\psi}{\mathbf{D}t} + \psi.\nabla u_f\right)\tau_p^2\right) \tag{2.11}$$

$$\eta = \frac{3}{2s+1} \tag{2.12}$$

η is the density ratio. With η=0.0, equation (2.11) reverts back to equation (2.9). Finally, the particle velocity v_p is approximated in terms of local fluid velocity u_f and its spatial and temporal derivatives.

2.5.1 Scalar equation for sediment concentration in FEM

It is recalled from Winterwerp [2001] that if the settling velocity w_s of fine sediment particles is much lower than vertical velocity fluctuations $w_s << v_{RMS}$, in the range $0.1mm/s < w_s < 2mm/s$, the single-phase formulation is applicable. The sediment concentration must be also low. Here, we focus on the Euler-Euler single-phase or mixture model [Zhu et al., 2013] in which each fine particulate phase follows the movement of the fluid flow except for the settling velocity.
Ferry and Balachandar [2001] demonstrated applicability of the FEM in the two-way coupling framework meaning the volumetric loading is extremely below unity. Accordingly, the conservation equation for the sediment concentration is,

$$\frac{\partial C}{\partial t} + \nabla.\left(Cv_p\right) = 0.0 \tag{2.13}$$

It has to be noticed that diffusive term relating to the volumetric concentration is neglected in equation (2.13). After introducing expansion equation (2.11) into equation (2.13), we get a simplified closed system of the concentration balance,

$$\frac{DC}{Dt} = (1-\eta)\,\tau_p\nabla.\left(C\left(\frac{Du_f}{Dt} - g\right)\right) \tag{2.14}$$

It is interesting to acknowledge that the settling velocity term is appeared in equation (2.14). Here, we implement some simplifications in equation (2.14) while sustaining the diffusive part. Consequently, proposed advection-diffusion equation (2.15) for the volumetric concentration C as the scalar field is [Dallali and Armenio, 2015],

$$\frac{\partial C}{\partial t} + \frac{\partial}{\partial x_j}\left[\left(u_j - w_s\delta_{j2}\right)C\right] = \epsilon\frac{\partial^2 C}{\partial x_j \partial x_j} \tag{2.15}$$

$$\epsilon = \frac{\nu}{Sc} \tag{2.16}$$

ϵ is the molecular diffusivity or molecular diffusion coefficient for sediment particles. Sc is the molecular Schmidt number which is equal to unity [Dallali and Armenio, 2015]. And, δ_{ij} is the Kronecker delta. Since the settling velocity term is defined in the scalar transport equation (2.15), one-way coupling is regarded in this study. Moreover, because a highly turbulent open channel flow is investigated in this study, the turbulent eddy diffusivity may be much higher than the molecular one in equation (2.15).

2.5.1.1 Rouse equation

The vertical distribution of the eddy viscosity in uniform unidirectional open channel flows can be determined by [Cellino, 1998],

$$\nu_t = \kappa u_* \frac{y}{h}(h - y) \tag{2.17}$$

h, κ and u_* are the water depth, von Karman constant and shear velocity, respectively. It could be also expressed using the log-law as [Nezu and Nakagawa, 1993],

$$\nu_t = -\frac{\langle u'v' \rangle}{\left(\frac{\partial \langle U \rangle}{\partial y}\right)} \tag{2.18}$$

$\langle u'v' \rangle$ is the depth-averaged Reynolds stress and $\langle U \rangle$ is the depth-averaged streamwise velocity. Coleman [1981] comprehended that the von Karman constant ($\kappa = 0.4$) remains unchanged for both clear water case (CWC) and sediment-laden flow (SLF). It is recalled here that the eddy diffusivity and eddy viscosity are assumed to be identical. When substituting equation (2.17) into equation (2.26), the well-known Rouse equation [Cellino, 1998] being valid in the range $a < y < h$, can be derived,

$$\frac{C}{C_{ref}} = \left(\frac{h - y}{y}\frac{a}{h - a}\right)^{\alpha} \tag{2.19}$$

$$\alpha = \frac{w_s}{\kappa u_*} \tag{2.20}$$

α is the Rouse number. It is understood that C_{ref} which is computed on a layer of sediment with the height of $a = 0.05 \times h$. It quantifies the erosion rate from the channel bed. For $y > a$, sediment particles are transported in the suspension mode whereas for $y < a$, sediments are part of the bed-load. When a sediment-laden flow manifests this distribution of the sediment concentration, suspended matter is in the full capacity. It means any further insertion of sediment particles into the flow field results in the deposition of sediment particles without any augmentation of the suspended load.
Pay attention that the steady-state condition, one dimensionality of the sediment concentration and single settling velocity in deriving Rouse equation are assumed.

2.5.2 Continuity equation in FEM

Some assumptions are taken regarding the derivation of the two-way coupled equations in the FEM. There is no volume transfer between phases. Ferry and Balachandar [2001] wrote a balance for total mass of a system within an arbitrary control volume in the limit of small volumetric loading ($C << 1$). Since the fluid is incompressible and there are insignificant density variations, velocity field is solenoidal or divergence-free. Mass conservation or continuity equation is,

$$\frac{\partial u}{\partial x} + \frac{\partial v}{\partial y} + \frac{\partial w}{\partial z} = 0 \Leftrightarrow \frac{\partial u_j}{\partial x_j} = 0 \tag{2.21}$$

Indexes j=1, 2 and 3 represent the streamwise, wall-normal and spanwise directions, respectively. x_1, x_2 and x_3 also refer to x, y and z, respectively. Moreover, velocities u_1, u_2 and u_3 represent u, v and w, respectively.

2.5.3 Navier-Stokes (NS) equations in FEM

The Navier-Stokes equations [Dey, 2014] for an incompressible viscous Newtonian fluid [Pope, 2000] in Cartesian coordinate are illustrated by [Fakhari, 2015],

$$\frac{\partial u_i}{\partial t} + \frac{\partial \left(u_i u_j\right)}{\partial x_j} = -\frac{1}{\chi \rho_0}\frac{\partial p}{\partial x_i} + \frac{\nu}{\chi}\frac{\partial^2 u_i}{\partial x_j \partial x_j} + \frac{1}{\chi}\Pi - g_m \delta_{i2} \tag{2.22}$$

The Boussinesq approximation [Armenio and Sarkar, 2002] is valid here because the density variation is small with respect to the reference density ρ_0 which is the density of water. Π is the imposed mass flow rate or pressure gradient divided by ρ_0 for open channel flows. ν is the kinematic viscosity of fluid and p is the hydrodynamic pressure. The coefficient χ is measured by,

$$\chi = 1 + (s-1)\, C \tag{2.23}$$

Note that for the clear water flow, we have $\chi = 1.0$. Although the volumetric loading (C) is small, the mass loading (ρC) is not. Ferry and Balachandar [2001] communicated that main effect of the particulate phase on the momentum equation is to introduce the mixture density,

$$\rho_m = \chi \rho_0 \tag{2.24}$$

It can be interpreted that suspended particles are in the equilibrium. Though, the particle velocity in the FEM is different from the fluid velocity. Though, their acceleration is same. Similarly, Winterwerp [2001] and Dallali and Armenio [2015] stated that to account for effects of the sediment concentration on hydrodynamics of the flow or two-way coupling, a modified gravity term g_m must be introduced in the NS equations,

$$g_m = (\chi - 1)\, g \tag{2.25}$$

2.6 Boundary condition for sediment concentration

Since the turbulent field is homogeneous in the streamwise (x) as well as spanwise directions (z), the periodic boundary condition is imposed for the velocity, pressure and sediment concentration fields. One of important steps in modeling SST is the definition of the boundary condition for the sediment concentration at the free surface and bottom wall.

2.6.1 Free surface

Equation (2.15) represents the distribution of the suspended sediment concentration by considering an advection-diffusion equation in a general form. This can be simplified if there is a steady-state condition with no change of the sediment concentration in x (streamwise) and z (spanwise) directions, [Cellino, 1998] [Graf and Cellino, 2002],

$$w_s C + \epsilon \frac{\partial C}{\partial y} = 0.0 \tag{2.26}$$

In the mixture model, the streamwise velocity of the fluid is equivalent to that of sediment particles. Though the vertical velocity of sediment particles is equal to the settling velocity of a single particle in a pure still clear water. Furthermore, the molecular diffusion coefficient ϵ_t for the sediment concentration goes to zero at the free surface.
Cellino [1998] and Graf and Cellino [2002] indicated that equation (2.26) is valid when the volumetric concentration is small $C < 0.05$. Pay attention that Bai et al. [2013] considered the sum of the molecular and turbulent diffusivities $\epsilon_{tot} = \epsilon + \epsilon_t$ instead of ϵ for the boundary condition of the sediment concentration at the free surface.

2.6.2 Channel bed

From a physical perspective, sediments are entrained into the flow when the shear stress gets higher than its critical value. Thus, the bed boundary condition for the sediment concentration should outline this entrainment arising from excess shear stress. Additionally, because of the settling velocity of sediment particles and stratification effects, there is a hyper concentration layer close to the channel bed so that scalar equation (2.15) fails to accurately account for the sediment concentration. Therefore, in the literature multitudinous empirical reference concentration C_{ref} formulations and pick-up rate functions are proposed to parameterize this region. Zedler and Street [2006] stated that the reference concentration formula were developed for flows in the equilibrium condition and hence they may not be appropriate for unsteady flows. Besides, they are sensitive to the reference height. The alternative procedure is the pick-up rate function which was developed to model the unsteady sediment transport.

However, Villaret and Davies [1995] established that these reference concentration formula had been used mainly to assess the instantaneous volumetric concentration in unsteady problems. Preference of the pick-up rate function over the reference concentration formula is a subject of discussion. Hence, here we adopt the reference concentration formulation derived by Smith and Mclean [1977],

$$C_{ref} = C_0 \frac{\gamma_0 S_0}{1 + \gamma_0 S_0} \tag{2.27}$$

$$S_0 = \frac{\tau_w - \tau_{cr}}{\tau_{cr}} \tag{2.28}$$

It has to be emphasized that corresponding values of γ_0 and C_0 are 2.4×10^{-3} and 0.65, respectively. C_0 is the maximum of the concentration of sediment particles. C_{ref} depends on the temporal bed shear stress and critical bed shear stress. The erosion is absent when the bed shear stress is lower than critical one. Practically speaking, C_{ref}, which is assumed at $0.05 \times h$, represents the potential of the turbulent flow to keep sediment particles in the suspension mode.

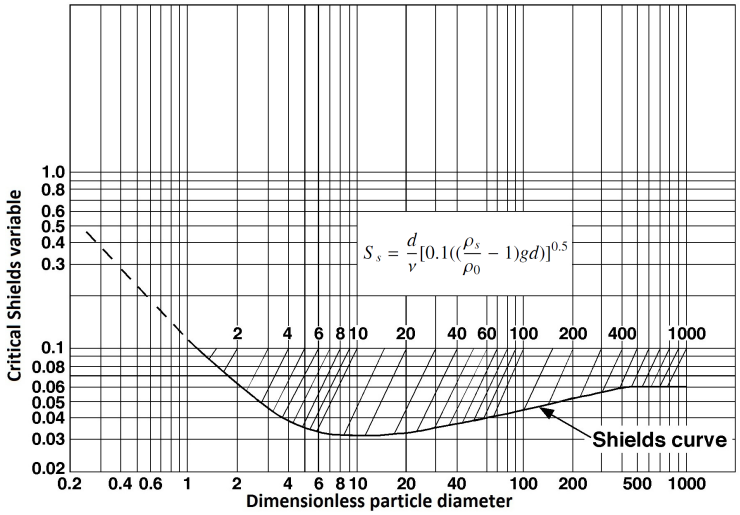

Figure 2.2 – Shields diagram together with proposal of Vanoni [1975]

Figure (2.2) depicts the Shields diagram. It shows relationships between dimensionless particle diameter d^* and critical bed shear stress τ_{cr} or critical Shields variable θ_{cr},

$$\theta_{cr} = \frac{\tau_{cr}}{(\rho_s - \rho_0)\, gd} \tag{2.29}$$

$$d^* = \frac{u_* d}{\nu} \tag{2.30}$$

Dallali and Armenio [2015] declared that the Shields diagram underestimates the critical bed shear stress. To overcome this in the suspension mode, Vanoni

[1975] introduced an upper limit shown by inclined lines in figure (2.2),

$$S_s = \frac{d}{\nu}\left[0.1\left(\left(\frac{\rho_s}{\rho_0} - 1\right) gd\right)\right]^{0.5} \tag{2.31}$$

Keep in mind that the temporal shear stress on the channel bed is obtained form corresponding components in streamwise (x) and spanwise (z) directions,

$$\tau_w = \sqrt{\tau_x^2 + \tau_z^2} \tag{2.32}$$

Chapter 3

Large eddy simulation (LES)

3.1 Generalities on turbulence

Based on relative importance of viscous and inertia forces, fluid flows can be classified into laminar, turbulent and transitional. Laminar or streamline flow takes place when the velocity and flow depth are low. It is seen as a layered flow in which layers of fluid slide over each other. Concerning hydraulics of open channel flows, the laminar flow does not happen from a practical point of view. The transitional regime happens when the Reynolds number is in this range,

$$2300 < Re = \frac{4R_h U}{\nu} < 4500 \tag{3.1}$$

As the velocity of the flow enhances more, the laminar flow gets highly unstable and instantaneous eddies form in the flow. This three-dimensional (3D) irregular and fluctuating behavior of fluid particles in free shear and wall-bounded flows is called turbulence [Pope, 2000]. The large-scale movements are significantly affected by the boundary condition and they are mainly responsible for transport and mixing. In contrast to the laminar flow, mixing and transport of fluid parcels in turbulent flows are highly effective. On contrary, small-scale eddies, which have a universal behavior and are independent of the geometry, dissipate the energy which is received from large-scale eddies by viscosity.
The turbulent flows are grouped into three classes, smooth turbulent flows, fully rough turbulent flows and transitional turbulent flows. Shifting from smooth turbulent flow to fully rough turbulent flow is quite different from the moment when the laminar flow gets turbulent. The transition between the smooth turbulent flow and fully turbulent flow depends on the Reynolds number Re and roughness height k. As the size of roughness elements gets bigger and approaches the flow depth or hydraulic radius, flow is called macro-rough flow. Water surface may be disturbed for lateral macro-rough flows. In the smooth

turbulent open channel flow, roughness elements are adequately tiny that are located inside the viscous boundary layer. In the fully rough turbulent flow, roughness elements are big enough to be inside the turbulent boundary layer (TBL).
If the Reynolds number Re is in low-to-moderate range, governing equations could be solved by the direct numerical simulation (DNS) [Kim et al., 1987] using fine meshing. This method is completely free of any modeling assumptions and all lengthscales and timescales of the flow down to the Kolmogorov scale should be computed and computational cost elevates by Re^3 correspondingly. DNS provides an improved knowledge of the physics of turbulent flows such as the role of the coherent structures.
Reynolds Averaged Navier-Stokes equations (RANS) are frequently used in applied engineering, although the accuracy of the simulation depends on the closure model. It may require tuning of model constants.
Large-eddy simulations (LES) constitute an intermediate approach between DNS and RANS. In the LES, large-scales, energy-carrying, structures are resolved while more isotropic, small scales, are modeled using a subgrid-scales (SGS) model. The scale separation in the LES is accomplished using the filtering operation. Depending on the treatment of the viscous sub-layer in wall-bounded flows, there are two variations of the LES, wall-resolving LES and unresolved wall-function LES.
In the wall-resolving LES, the resolution is comparable to the DNS while in the unresolved wall-function LES, a coarse grid is used. Nodes next to the wall are modeled with a wall function which mimics the presence of a solid wall.

3.2 Filtering operation in LES

To solve governing equations of turbulent open channel flows (TOCF), the large eddy simulation (LES) becomes an alternative. Large scale eddies, figure (3.1), are directly resolved and smaller scales, figure (3.1) are parameterized using subgrid scale (SGS) models. In the LES, the scale separation is accomplished by

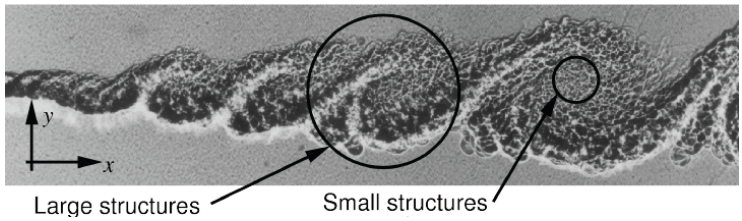

Figure 3.1 – Depiction of wide-range eddies in the flow taken from [Brown and Roshko, 1974]

using a low-pass filtering [Leonard, 1974] operation in which the filtered velocity field could be applied on a coarse grid. Taking for instance $\mathbf{Z}$ as a turbulent

variable, the grid filtering operation is defined as,

$$\overline{Z}\left(\mathbf{x},t\right)=\int\overline{G}(r,\mathbf{x})\mathbf{Z}\left(\mathbf{x}-r,t\right)dr \tag{3.2}$$

$\mathbf{x}$ in equation (3.2) manifests general spatial positioning (x,y,z). Keep in mind that the integration is extended to the entire flow domain and selected grid filter kernel $\overline{G}(r,\mathbf{x})$, which specifies the size and structure of small eddies, has to satisfy the normalization condition [Pope, 2000]. In the LES, each variable $\mathbf{Z}\left(\mathbf{x},t\right)$ is divided into two parts, filtered part $\overline{Z}\left(\mathbf{x},t\right)$ and residual (SGS) part $z'\left(\mathbf{x},t\right)$ like,

$$\mathbf{Z}\left(\mathbf{x},t\right)=\overline{Z}\left(\mathbf{x},t\right)+z'\left(\mathbf{x},t\right) \tag{3.3}$$

Based on the Reynolds decomposition [Guo and Julien, 2001], each variable is composed of the time-averaged $Z\left(\mathbf{x},t\right)$ and fluctuating parts $z\left(\mathbf{x},t\right)$,

$$\mathbf{Z}\left(\mathbf{x},t\right)=Z\left(\mathbf{x},t\right)+z\left(\mathbf{x},t\right) \tag{3.4}$$

While time-averaging of the fluctuation part z is zero, filtering the residual (SGS) part $\overline{z'}$ is not necessarily zero.
Multifarious types of the filter function are proposed and the top-hat filter [Ghosal and Moin, 1995] is used,

$$G(r)=\begin{cases}\dfrac{1}{\overline{\Delta}}, & \text{if } \mid r\mid<\dfrac{\overline{\Delta}}{2}\\ 0, & \text{otherwise}\end{cases} \tag{3.5}$$

$\overline{\Delta}$ is the smoothing operator or filter width. It plays a key role in modeling of unresolved stresses. Depending on the SGS model implemented, various smoothing operators in the LES were proposed.

3.3 Filtered governing equations

Considering the two-phase coupled equations in the FEM, when all turbulent variables velocity, pressure and concentration are specified in terms of their corresponding filtered and SGS components, following filtered governing equations could be gained,

$$\frac{\partial\overline{u}_j}{\partial x_j}=0 \tag{3.6}$$

$$\frac{\partial\overline{u}_i}{\partial t}+\frac{\partial\left(\overline{u}_i\overline{u}_j\right)}{\partial x_j}=-\frac{1}{\chi\rho_0}\frac{\partial\overline{p}}{\partial x_i}+\frac{\nu}{\chi}\frac{\partial^2\overline{u}_i}{\partial x_j\partial x_j}+\frac{1}{\chi}\Pi-g_m\delta_{i2}-\frac{\partial\tau_{ij}}{\partial x_j} \tag{3.7}$$

$$\frac{\partial\overline{C}}{\partial t}+\frac{\partial}{\partial x_j}\left[\left(\overline{u}_j-w_s\delta_{j2}\right)\overline{C}\right]=\epsilon\frac{\partial^2\overline{C}}{\partial x_j\partial x_j}-\frac{\partial\omega_j}{\partial x_j} \tag{3.8}$$

The influences of smaller scales are represented by SGS stresses τ_{ij} and SGS turbulent fluxes for the concentration ω_j,

$$\tau_{ij}=\overline{u_iu_j}-\overline{u}_i\overline{u}_j \tag{3.9}$$

$$\omega_j = \overline{u_j C} - \overline{u}_j \overline{C} \tag{3.10}$$

Utilizing the gradient diffusion hypothesis [Bai et al., 2013], the SGS sediment flux is estimated by,

$$\omega_j = -\epsilon_t \frac{\partial \overline{C}}{\partial x_j}, \epsilon_t = \frac{\nu_t}{Sc_t} \tag{3.11}$$

ϵ_t is the SGS concentration diffusivity. Sc_t is the turbulent Schmidt number. Theses appeared terms should be modeled using SGS models for momentum and concentration equations. As stated by Piomelli and Balaras [2002], SGS terms just contribute a small fraction of total turbulent stresses.

3.4 SGS models

In the literature, there are many SGS models for treating SGS stresses and turbulent fluxes for the scalar field. As Germano et al. [1991] elucidated, majority of models to treat SGS stresses is based on the eddy viscosity. Smagorinsky model can be applied to account for both SGS stress and turbulent fluxes for the concentration. A single, universal constant is assumed in the Smagorinsky model to compute the eddy viscosity. Though, it is impractical for modeling various phenomena in flows. This model cannot take into account energy transfer from small scales to large scales or backscatter. And, SGS stresses may not disappear at wall. Modifications to the Smagorinsky model were made close to walls in channel flows in order to vanish SGS stresses at walls. Also, the eddy viscosity and state of the flow must be determined locally. For example, while a dynamic eddy viscosity model developed by Armenio and Piomelli [2000] can be implemented to compute SGS stresses, a dynamic eddy diffusivity model proposed by Armenio and Sarkar [2002] can be used to compute SGS turbulent fluxes for the concentration.

3.4.1 Smagorinsky model

In the isotropic Smagorinsky model [Smagorinsky, 1963], it is assumed that small scales of the motion are in the equilibrium and there is a balance between production and dissipation of the turbulent energy. The eddy viscosity ν_t is calculated from,

$$\nu_t = \left(C_s \overline{\Delta}\right)^2 \mid \overline{S} \mid \tag{3.12}$$

$\overline{\Delta}$ is the grid filter width. The Deardroff equivalent length scale [Roman et al., 2010] is commonly used for the unequal-sided cells,

$$\overline{\Delta} = (\Delta x \Delta y \Delta z)^{0.33} \tag{3.13}$$

C_s is Smagorinsky constant in range $0.065 < C_s < 0.2$. The large-scale strain-rate tensor $\mid \overline{S} \mid$ is taken from

$$\mid \overline{S} \mid = \left(2\overline{S}_{ij}\overline{S}_{ij}\right)^{0.5} \tag{3.14}$$

The appearing components are defined by,

$$\overline{S}_{ij} = \frac{1}{2}\left(\frac{\partial \overline{u}_i}{\partial x_j} + \frac{\partial \overline{u}_j}{\partial x_i}\right) \tag{3.15}$$

Eventually, SGS stresses, last term in equation (3.7), which represent influences of small-scale motions, could be computed from,

$$\tau_{ij} = -2\nu_t \overline{S}_{ij} \tag{3.16}$$

The Smagorinsky model can be applied to calculate the SGS sediment flux $\overline{\omega}_j$ like the study of the wave-induced sediment transport done by Gilbert et al. [2007]. In this study, the turbulent Schmidt number Sc_t is set to unity $\nu_t = \epsilon_t$ and Smagorinsky constant C_s for both momentum and concentration equations is same. Nevertheless, Le Ribault et al. [2001] and Horiuti [1992] speculated that the constant for the concentration equation must be bigger than that for the momentum equation.
The Smagorinsky constant is a highly flow-dependent coefficient [Bai et al., 2013]. Physically speaking, the eddy viscosity must be zero close to walls. In the Smagorinsky model, it is not because the strain-rate tensor is big as a disadvantage. Smagorinsky model also cannot justify the energy transfer from small scales to large scales or backscatter. Accordingly, researchers have introduced various strategies like the dynamic Smagorinsky model (DSM) to force SGS stresses to vanish at walls of channel flows.

3.4.2 Dynamic eddy viscosity model

In dynamic SGS models, model coefficients are estimated dynamically in each cell. It depends on the energy content of smallest resolved scales rather than inputting a fixed constant. All inefficiencies of the fixed-coefficient model or Smagorinsky model could be removed because the coefficient disappears in laminar flows as well as close to walls. To accomplish this, like equation (3.2), a test filtering operation is done by,

$$\widehat{Z}\left(\mathbf{x}, t\right) = \int \widehat{G}(r, \mathbf{x}) \mathbf{Z}\left(\mathbf{x} - r, t\right) dr \tag{3.17}$$

Germano et al. [1991] stated that new filter kernel is selected as,

$$\widehat{\overline{G}}(r, \mathbf{x}) = \widehat{G}(r, \mathbf{x}) \overline{G}(r, \mathbf{x}) \tag{3.18}$$

Once we apply the filtering kernel $\widehat{\overline{G}}(r, \mathbf{x})$, new versions of the filtered continuity and Navier-Stokes equations could be realized,

$$\frac{\partial \widehat{\overline{u}}_j}{\partial x_j} = 0 \tag{3.19}$$

$$\frac{\partial \widehat{\overline{u}}_i}{\partial t} + \frac{\partial\left(\widehat{\overline{u}}_i \widehat{\overline{u}}_j\right)}{\partial x_j} = -\frac{1}{\chi \rho_0}\frac{\partial \widehat{\overline{p}}}{\partial x_i} + \frac{\nu}{\chi}\frac{\partial^2 \widehat{\overline{u}}_i}{\partial x_j \partial x_j} + \frac{1}{\chi}\Pi - g_m \delta_{i2} - \frac{\partial T_{ij}}{\partial x_j} \tag{3.20}$$

Note that the test filter is supposed to be twice of the grid filter,

$$\widehat{\Delta} = 2\overline{\Delta} = 2\left(\Delta x \Delta y \Delta z\right)^{0.33} \tag{3.21}$$

The SGS stresses T_{ij} are explained by,

$$T_{ij} = \widehat{\overline{u_i}\overline{u_j}} - \widehat{\overline{u}}_i \widehat{\overline{u}}_j \tag{3.22}$$

The resolved turbulent stresses Γ_{ij} are specified by,

$$\Gamma_{ij} = \widehat{\overline{u_i}\overline{u_j}} - \widehat{\overline{u}}_i \widehat{\overline{u}}_j \tag{3.23}$$

The stresses Γ_{ij} [Germano et al., 1991] could be measured explicitly. They are indicative of contribution to SGS stresses by scales whose length is considered intermediate between $\overline{\Delta}$ and $\widehat{\Delta}$. The identity between these stresses is,

$$T_{ij} = \Gamma_{ij} + \widehat{\tau}_{ij} \tag{3.24}$$

This identity equation (3.24) could be utilized to obtain the Smagorinsky coefficient depending on the type of turbulent flows. To parameterize both T_{ij} and SGS stresses τ_{ij} in the Smagorinsky model, assume M_{ij} and m_{ij} designating anisotropic parts of T_{ij} and τ_{ij}, respectively,

$$\tau_{ij} - \left(\frac{\delta_{ij}}{3}\right)\tau_{kk} \simeq m_{ij} = -2C_{ds}\overline{\Delta}^2 \mid \overline{S} \mid \overline{S}_{ij} \tag{3.25}$$

$$T_{ij} - \left(\frac{\delta_{ij}}{3}\right)T_{kk} \simeq M_{ij} = -2\widehat{\overline{\Delta}}^2 \mid \widehat{\overline{S}} \mid \widehat{\overline{S}}_{ij} \tag{3.26}$$

$$\mid \widehat{\overline{S}} \mid = \left(2\widehat{\overline{S}}_{mn}\widehat{\overline{S}}_{mn}\right)^{0.5}, \widehat{\overline{S}}_{ij} = \frac{1}{2}\left(\frac{\partial \widehat{\overline{u}}_i}{\partial x_j} + \frac{\partial \widehat{\overline{u}}_j}{\partial x_i}\right) \tag{3.27}$$

It should be emphasized that $\widehat{\overline{\Delta}}$ is the filter width related to $\widehat{\overline{G}}(r, \mathbf{x})$.
When replacing equations (3.25) and (3.26) in the identity equation, we get a dynamic constant C_{ds} over parallel planes (shown by <>) to the wall [Germano et al., 1991],

$$C_{ds} = -\frac{1}{2}\frac{\left\langle \Gamma_{kl}\overline{S}_{kl}\right\rangle}{\widehat{\overline{\Delta}}^2\left\langle \mid \widehat{\overline{S}} \mid \widehat{\overline{S}}_{mn}\overline{S}_{mn}\right\rangle - \overline{\Delta}^2\left\langle \mid \widehat{\overline{S}} \mid \widehat{\overline{S}}_{pq}\overline{S}_{pq}\right\rangle} \tag{3.28}$$

An error [Foroozani, 2015] appears in this substitution which can be minimized using the least-squares approach [Lilly, 1992]. Finally, the coefficient is calculated dynamically [Foroozani, 2015],

$$C_{ds} = -\frac{1}{2}\frac{\langle \Gamma_{ij}M_{ij}\rangle}{\langle M_{ij}M_{ij}\rangle} \tag{3.29}$$

3.4.3 Dynamic eddy diffusivity model

Le Ribault et al. [2001] applied the LES with the dynamic eddy diffusivity model for the scalar transport in a plane jet. In the sediment-laden flow, the SGS concentration flux is retained like [Armenio and Sarkar, 2002],

$$\omega_j = -C_\rho \overline{\Delta}^2 \mid \overline{S} \mid \frac{\partial \overline{C}}{\partial x_j} \tag{3.30}$$

Analogous to the dynamic eddy viscosity model, constant C_ρ could be ascertained utilizing grid and test filters in the concentration equation,

$$C_\rho = -\frac{1}{2} \frac{\langle \Lambda_i \Upsilon_i \rangle}{\langle \Upsilon_k \Upsilon_k \rangle} \tag{3.31}$$

According to Armenio and Sarkar [2002], corresponding resolved SGS sediment fluxes Λ_i and anisotropic part Υ_i are characterized by,

$$\Lambda_i = \widehat{\overline{C}\overline{u}_i} - \widehat{\overline{C}}\widehat{\overline{u}}_i \tag{3.32}$$

$$\Upsilon_i = \widehat{\overline{\Delta}}^2 \mid \widehat{\overline{S}} \mid \widehat{\frac{\partial \overline{C}}{\partial x_i}} - \overline{\overline{\Delta}^2 \mid \overline{S} \mid \frac{\partial \overline{C}}{\partial x_i}} \tag{3.33}$$

To prevent unphysical back-scattering [Armenio and Sarkar, 2002], dynamic coefficients are equal to zero when they get negative.

3.5 Unresolved wall-function LES

There are two distinct ways to treat wall-bounded flows using the LES called near-wall resolution (LES-NWR) and near-wall modeling (LES-NWM). Considering smooth walls, if the grid and filter are selected so that nearly 80 percent of the energy everywhere including in the viscous sub-layer are resolved, the consequence is a LES with the near wall resolution. This method necessitates a very fine grid close to walls especially in very high Reynolds number flows in aeronautical and meteorological applications. Hence, it is highly expensive from a computational cost point of view.
Chapman [1979] theorized that resolving the inner layer (il) in a plane channel flow needs this meshing,

$$(N_x N_y N_z)_{il} \propto Re^{1.8} \tag{3.34}$$

In the outer layer (ol), in which the the direct influence of the viscosity on the mean velocity is insignificant, the resolution is less demanding,

$$(N_x N_y N_z)_{ol} \propto Re^{0.4} \tag{3.35}$$

Piomelli [2008] visually clarified that even at moderate $Re = 10^4$ over 50 percent of computer resources has be used to resolve just 10 percent of the flow.
The alternative is to use the LES-NWM in which the inner layer is bypassed

and its effects are modeled in a global sense. The grid size in the LES-NWM may be reckoned by outer-flow eddies and the cost of calculation becomes negligibly dependent on Re. The model should be able to determine the wall shear stress to the outer layer. The grid chosen close to walls is too coarse to solve small-scale motions contributing to the momentum transfer. Time-step is much bigger than the time-scale of these motions so the filtering operation becomes almost identical to the Reynolds averaging as established by Piomelli and Balaras [2002] and Piomelli [2008].

There are many wall-layer models proposed for channel flows but here the equilibrium stress model is adopted. Deardorff [1970] and Schumann [1975] firstly bypassed the inner layer by assuming an equilibrium layer in which stress is constant. This approximate boundary condition may be applied in environmental and geophysical flows where the geometry is so simple and Re can be high. It has to be kept in mind that corrections [Piomelli, 2008] to this model may be accomplished when considering stratification effects or roughness.

Assuming a constant stress layer near the bottom smooth wall implies that horizontal velocities at the first grid off the bottom wall and in the outer layer (ol) satisfies a logarithmic profile [Piomelli, 2008],

$$\Psi_1^+ = \frac{\Psi_1}{u_*} = \frac{1}{\kappa} log\left(y_1^+\right) + B \tag{3.36}$$

$$y_1^+ = \frac{y_1 u_*}{\nu} \tag{3.37}$$

Note that variables with superscript + are shown in wall units. Ψ_1 is the modulus of the velocity at the first node off the bottom wall. It is obtained from,

$$\Psi_1(x, y_1, z, t) = \sqrt{u^2(x, y_1, z, t) + w^2(x, y_1, z, t)} \tag{3.38}$$

Assuming the clear water flow, the von Karman constant κ is equal to 0.41 and constant is $B = 5.1$.

Piomelli [2008] commented that if the vertical position of the first node in wall units (y_1^+) is lower than 11.0, the logarithmic law switches to the linear law $\Psi_1^+ = y_1^+$. From this law-of-the-wall, the friction velocity is computed based on y_1^+ and accordingly, the wall shear stress is obtained from the friction velocity by,

$$\tau_w = \rho_0 u_*^2 \tag{3.39}$$

Deardorff [1970] defined second-order derivatives of filtered streamwise ($\overline{u}$) and spanwise ($\overline{w}$) velocities in a turbulent channel flow at infinite Re,

$$\frac{\partial^2 \overline{u}}{\partial y^2} = -\frac{1}{\kappa y_1^2} + \frac{\partial^2 \overline{u}}{\partial z^2} \tag{3.40}$$

$$\frac{\partial^2 \overline{w}}{\partial y^2} = \frac{\partial^2 \overline{w}}{\partial x^2} \tag{3.41}$$

Equation (3.40) forces the average velocity over the horizontal plane at the first node off the bottom wall to satisfy the logarithmic law. Normalization of all

variables in equations (3.40) and (3.41) can be done by the friction velocity and viscosity.

Schumann [1975] calculated the mean shear stress from the momentum balance equation. Wall shear stress is iteratively balanced by the imposed pressure gradient in channel flows. Schumann [1975] proposed following boundary conditions to relate the plane-averaged wall shear stress $\langle \tau_w \rangle_{xz}$ to Ψ_1 at the first node in channel flows,

$$\tau_{w,x}(x,z,t) = \left[\frac{\langle \tau_w \rangle_{xz}}{\Psi_1}\right] \overline{u}(x,y_1,z,t) \tag{3.42}$$

$$\tau_{w,z}(x,z,t) = \left[\frac{\langle \tau_w \rangle_{xz}}{\Psi_1}\right] \overline{w}(x,y_1,z,t) \tag{3.43}$$

It is obvious that $\overline{u}(x,y_1,z,t)$ and $\overline{w}(x,y_1,z,t)$ are temporal filtered velocity components at the first node off the bottom wall. The equilibrium stress model is applicable where the turbulence is in the equilibrium. Geometry of the flow under investigation is simple.

Piomelli and Balaras [2002] set cost of computations using the equilibrium stress model as $Re^{0.5}$. It is known that the Smagorinsky model may not be appropriate in reproducing correctly the eddy viscosity near the bottom smooth wall. Although velocity gradient terms are derived from the no-slip condition, they are wrongfully non-zero. In this regard, the strain rate tensor must be carefully analyzed to apply a proper SGS eddy viscosity at smooth walls in the Smagorinsky model. If the first computational node off the bottom smooth wall is positioned in the logarithmic region, corresponding prevailing terms in the strain rate tensor are prescribed by [Fakhari, 2015],

$$\overline{S}_{12} = \frac{u_*}{\kappa y_1}\frac{u(x,y,z,t)}{u(x,y_1,z,t)} \tag{3.44}$$

$$\overline{S}_{32} = \frac{u_*}{\kappa y_1}\frac{w(x,y,z,t)}{u(x,y_1,z,t)} \tag{3.45}$$

If the first computational node is located in the viscous layer, dominant terms are,

$$\overline{S}_{12} = \frac{u_*^2}{\nu}\frac{u(x,y,z,t)}{u(x,y_1,z,t)} \tag{3.46}$$

$$\overline{S}_{32} = \frac{u_*^2}{\nu}\frac{w(x,y,z,t)}{u(x,y_1,z,t)} \tag{3.47}$$

For flows over a rough surface with a constant roughness height k_s, the velocity is expressed by [Fakhari, 2015],

$$\Psi_1^+ = \frac{1}{\kappa} ln\left(\frac{y_1}{k_s}\right), y_1 > k_s \tag{3.48}$$

As Shamloo and Pirzadeh [2015] discussed, if the ratio h/k_s is less than 10, the boundary layer theory collapses. When there are isolated roughness elements, flow patterns depend strongly on the pitch-to-height ratio [Cui et al., 2003].

Chapter 4

LES-COAST code

In this study, the LES-COAST code, which is available at the PhD school of Earth Science and Fluid Mechanics (ESFM) of University of Trieste (UNITS) is used to do the LES of the SST in a turbulent open channel flows. Mixture flow model is used.
The curvilinear forms of governing equations are integrated using a modified version of the finite-difference fractional-step method in a non-stggered grid. It was developed by Zang et al. [1994]. The spatial derivatives are performed using central second-order methods, except for advective terms treated by the third-order QUICK scheme. The integration over time is done utilizing the Adams-Bashforth scheme for convective and off-diagonal diffusive terms. For diagonal diffusive terms, Crank-Nicolson scheme is adopted. To solve the Poisson equation, a multigrid technique is used. Periodic boundary conditions are defined in the streamwise (x) and spanwise (z) directions. No-slip conditions are applied at stationary walls. Totally speaking, written algorithm has a second-order accuracy both in time and space.
The LES-COAST code found many applications in the wind-driven sea circulation [Petronio et al., 2013], water mixing and renewals in Barcelona harbor area [Galea et al., 2014], mobile bed [Kyrousi et al., 2016] using level-set method (LSM) and immersed boundary method (IBM), oil spill dispersion [Zanier et al., 2017] in coastal areas, cubical Rayleigh-Benard convection [Foroozani et al., 2017] and so forth.

4.1 Curvilinear coordinate

To simulate complicated flow geometries, curvilinear coordinates are preferred due to better managing of boundaries. The transformation from Cartesian coordinates x_i to curvilinear ones ξ_i is established. Under strong-conservation law form [Zang et al., 1994] two-phase coupled equations in the FEM are trans-

formed in curvilinear coordinates [Zang et al., 1994],

$$\frac{\partial \mathbf{U}_m}{\partial \xi_m} = 0 \tag{4.1}$$

$$\frac{\partial J^{-1} u_i}{\partial t} + \frac{\partial F_{im}}{\partial \xi_m} = J^{-1} B_i \tag{4.2}$$

The flux F_{im} takes this form [Zang et al., 1994],

$$F_{im} = \mathbf{U}_m u_i + \frac{J^{-1}}{\chi \rho_0} \frac{\partial \xi_m}{\partial x_i} p - \frac{\nu}{\chi} G^{mn} \frac{\partial u_i}{\partial \xi_n} \tag{4.3}$$

B_i manifests all other terms [Foroozani, 2015] like the modified gravity term g_m appearing in the Navier-Stokes equations (2.22). J^{-1} is the reciprocal of the Jacobian. It is equivalent to the volume of each cell. $\mathbf{U}_m$ represents the volume flux [Zang et al., 1994] and G^{mn} is the mesh skewness tensor,

$$\mathbf{U}_m = J^{-1} \frac{\partial \xi_m}{\partial x_j} u_j \tag{4.4}$$

$$J^{-1} = det \left(\frac{\partial x_i}{\partial \xi_j} \right) \tag{4.5}$$

$$G^{mn} = J^{-1} \frac{\partial \xi_m}{\partial x_j} \frac{\partial \xi_n}{\partial x_j} \tag{4.6}$$

When writing the advection-diffusion equation (2.15) for the volumetric concentration as the scalar field in curvilinear coordinates, we could get,

$$\frac{\partial J^{-1} C}{\partial t} + \frac{\partial \mathbf{U}_m C}{\partial \xi_m} = \frac{\partial}{\partial \xi_m} \left(\epsilon G^{mn} \frac{\partial C}{\partial \xi_n} \right) + Q_j \tag{4.7}$$

Q_2 represents the vertical convective flux. It is related to the settling velocity of sediments in curvilinear coordinates,

$$Q_j = \frac{\partial}{\partial \xi_m} \left[\frac{\partial J^{-1} \xi_m}{\partial x_j} \left(w_s \delta_{j2} \right) C \right] \tag{4.8}$$

4.2 Discretization

A non-staggered grid [Zang et al., 1994] is taken in this study. It means pressure and velocities are defined at the center of each cell. Volume fluxes are defined at central points of their corresponding faces of control volumes. Spatial discretizaion is done using the second-order centered finite difference method (FDM). A semi-implicit time advancement is accomplished utilizing the accurate explicit Adams-Bashforth scheme for convective and off-diagonal viscous terms.

Implicit Crank-Nicolson method is used for diagonal viscous terms. Accordingly, discretizations of the continuity and Navier-Stokes equations are done,

$$\frac{\partial \mathbf{U}_m}{\partial \xi_m} = 0.0 \tag{4.9}$$

$$\begin{aligned} J^{-1}\frac{u_i^{n+1}-u_i^n}{\Delta t} = \frac{3}{2}\left(X_i^n + Y_E\left(u_i^n\right) + B_i^n\right) - \\ \frac{1}{2}\left(X_i^{n-1} + Y_E\left(u_i^{n-1}\right) + B_i^{n-1}\right) + \\ R_i\left(p^{n+1}\right) + \frac{1}{2}\left(Y_I\left(u_i^{n+1}+u_i^n\right)\right) \end{aligned} \tag{4.10}$$

Superscript n depicts advancement in time. The time step Δt could be fixed or adaptive but it must satisfy minimum Courant-Friedrichs-Lewy (CFL) condition. X_i shows convective terms. R_i is the gradient operator for pressure gradient terms. Y_I characterizes implicitly treated diagonal viscous terms whereas Y_E are explicitly treated off-diagonal viscous terms. They all are,

$$X_i = -\frac{\partial}{\partial \xi_m}\left(\mathbf{U}_m u_i\right) \tag{4.11}$$

$$R_i = -\frac{\partial}{\partial \xi_m}\left(J^{-1}\frac{\partial \xi_m}{\partial x_i}\right) \tag{4.12}$$

$$D_I = -\frac{\partial}{\partial \xi_m}\left(\nu G^{mn}\frac{\partial}{\partial \xi_n}\right), m = n \tag{4.13}$$

$$D_E = -\frac{\partial}{\partial \xi_m}\left(\nu G^{mn}\frac{\partial}{\partial \xi_n}\right), m \neq n \tag{4.14}$$

Discretization of the concentration equation as the scalar field can be performed similarly.

4.3 Fractional step method

The numerical code LES-COAST solves governing equations using the fractional step method. In each iteration, two steps, predictor and corrector (projection) solutions, are done. For example, for Cartesian velocities, instead of directly computing u_i^{n+1}, an intermediate velocity u_i^* is introduced in the predictor step by,

$$\begin{aligned} \left(I - \frac{\Delta t}{2J^{-1}}\right)\left(u_i^* - u_i^n\right) = \frac{\Delta t}{J^{-1}}\left[\frac{3}{2}\left(X_i^n + Y_E\left(u_i^n\right) + B_i^n\right) - \right. \\ \left. \frac{1}{2}\left(X_i^{n-1} + Y_E\left(u_i^{n-1}\right) + B_i^{n-1}\right) + R_i\left(p^{n+1}\right) + \frac{1}{2}\left(Y_I\left(u_i^{n+1}+u_i^n\right)\right)\right] \end{aligned} \tag{4.15}$$

I is the identity matrix. In the second step, corrector, the velocity is updated and pressure is taken to enforce the continuity condition,

$$u_i^{n+1} - u_i^* = \frac{\Delta t}{J^{-1}} \left[R_i \left(\phi^{n+1} \right) \right] \tag{4.16}$$

As assumed by Zang et al. [1994], the intermediate velocity u_i^* is not restricted by the continuity condition. The projection variable ϕ is related to the pressure with,

$$R_i \left(p \right) = \left(J^{-1} - \frac{\Delta t}{2} Y_I \right) \left(\frac{R_i \left(\phi \right)}{J^{-1}} \right) \tag{4.17}$$

The intermediate volume flux $\mathbf{U}_m^*$ is defined like Zang et al. [1994],

$$\mathbf{U}_m^* = J^{-1} \left(\frac{\partial \xi_m}{\partial x_j} \right) u_j^* \tag{4.18}$$

Contravariant fluxes at successive time instant are determined by,

$$\mathbf{U}_m^{n+1} = \mathbf{U}_m^* - \Delta t \left(G^{mn} \frac{\delta \phi^{n+1}}{\delta \xi_n} \right) \tag{4.19}$$

It must be emphasized that u_j^* is defined at cell centers while contravariant fluxes $\mathbf{U}_m^*$ and $\mathbf{U}_m^{n+1}$ are specified on cell faces. To calculate $\mathbf{U}_m^*$ on cell face, u_j^* must be interpolated on corresponding cell face using the third-order accurate upwind quadratic interpolation. It is analogous to the QUICK scheme. Finally, the elliptic pressure Poisson equation for the projection variable ϕ^{n+1} is solved iteratively using the unstructured multigrid method [Perng and Street, 1989]. Smoothing relaxation algorithm called successive line over relaxation (SLOR) is used,

$$\frac{\partial}{\partial \xi_m} \left(G^{mn} \frac{\partial \phi^{n+1}}{\partial \xi_n} \right) = \frac{1}{\Delta t} \frac{\partial \mathbf{U}_m^*}{\partial \xi_m} \tag{4.20}$$

Regarding stability of the LES-COAST code, the Courant number could be fixed or changeable for the fixed time step Δt. The local CFL number is established using,

$$CFL = \left(\frac{| u_1 |}{\Delta x} + \frac{| u_2 |}{\Delta y} + \frac{| u_3 |}{\Delta z} \right) = \left(| \mathbf{U}_1 | + | \mathbf{U}_2 | + | \mathbf{U}_3 | \right) \frac{\Delta t}{J^{-1}} \tag{4.21}$$

Δx, Δy and Δz are the grid spacing in Cartesian coordinates (x,y,z). u_i are Cartesian velocities while $\mathbf{U}_i$ are contravariant fluxes in curvilinear coordinates.

4.4 Filtered equations in curvilinear coordinate

Filtering aforementioned governing equations in curvilinear coordinates yields,

$$\frac{\partial \overline{\mathbf{U}}_m}{\partial \xi_m} = 0 \tag{4.22}$$

$$\frac{\partial\overline{J^{-1}u_i}}{\partial t}+\frac{\partial\overline{\mathbf{U}_m u_i}}{\partial\xi_m}=-\frac{\partial}{\partial\xi_m}\left(\overline{\frac{1}{\chi\rho_0}\frac{\partial J^{-1}\xi_m}{\partial x_i}p}\right)-\frac{\partial}{\partial\xi_m}\frac{\partial\sigma_{mi}}{\partial x_i}+ \\ -\frac{\partial}{\partial\xi_m}\left(\overline{\frac{\nu}{\chi}G^{mn}\frac{\partial u_i}{\partial\xi_n}}\right)+\overline{J^{-1}B_i} \tag{4.23}$$

As communicated by Fakhari [2015], SGS stresses σ_{mi} in curvilinear coordinates is defined like corresponding SGS stresses τ_{ij} in Cartesian coordinates in equation (3.9),

$$\sigma_{mi}=\overline{\mathbf{U}_m u_i}-\overline{\mathbf{U}}_m\overline{u}_i=\overline{J^{-1}\frac{\partial\xi_m}{\partial x_j}u_j u_i}-\overline{J^{-1}\frac{\partial\xi_m}{\partial x_j}u_j\overline{u}_i} \tag{4.24}$$

SGS stress models demonstrated in Cartesian coordinates are also applicable in curvilinear coordinates. When doing the filtering of the concentration equation (4.7) in curvilinear coordinates, we obtain,

$$\frac{\partial\overline{J^{-1}C}}{\partial t}+\frac{\partial\overline{\mathbf{U}_m C}}{\partial\xi_m}=\frac{\partial}{\partial\xi_m}\left(\overline{\epsilon G^{mn}\frac{\partial C}{\partial\xi_n}}\right)+ \\ \frac{\partial}{\partial\xi_m}\left(\overline{\frac{\partial J^{-1}\xi_m}{\partial x_j}\left(w_s\delta_{j2}\right)C}\right)-\frac{\partial\xi_m}{\partial x_j}\frac{\partial\omega_j}{\partial\xi_m} \tag{4.25}$$

Chapter 5

Case study I: wall-resolving LES of SST

5.1 DNS-FEM for laminar sediment-laden flow

The accuracy of the code in solving two-phase coupled equations in the FEM is assessed using the direct numerical simulation (DNS) of a laminar close channel flow laden with sediment particles. The numerical results are compared against the analytic solution. The lengths of the close channel flow are,

$$L_x = 2\pi(m), L_y = 2(m), L_z = \frac{2\pi}{3}(m) \tag{5.1}$$

There is no effect of the sidewall or secondary flow on the SST. The number of cells is 32 in all directions. The flow is driven with a constant pressure gradient divided by the water density $\Pi = 1.0$ in the streamwise direction. The gravity term is deactivated and the density ratio between sediment particles and water in this laminar case is $s = 2.65$. In x and z directions, the periodic boundary condition for both momentum and scalar transport equations are specified. Smooth rigid walls are assumed on top and bottom boundaries. The Courant number, molecular Schmidt number, kinematic viscosity and time step are,

$$CFL = 0.5, Sc = 0.7, \nu = 0.1\frac{m^2}{s}, \Delta t = 1.96 \times 10^{-2} s \tag{5.2}$$

The fluid is incompressible and flow in the close channel is fully developed in the streamwise direction. Since the flow is constrained by parallel top and bottom plates, the vertical velocity is zero $v = 0.0$. Under these circumstances, the Navier-Stokes equation (2.22) is simplified,

$$\frac{1}{\chi}\Pi = \frac{\nu}{\chi}\frac{\partial^2 u}{\partial y^2} \tag{5.3}$$

It is apparent that Π is inherently negative. One significant finding here is that vertical profiles of the streamwise velocity u in both clear water and sediment-laden flows are equivalent regardless of the imposed concentration profile. Using integration twice, we could easily get the vertical profile of the streamwise velocity,

$$u\left(y\right) = \frac{1}{2\nu}\left(y^2 - 2hy\right)\Pi \tag{5.4}$$

Under the steady state condition, the vertical profile of the concentration is obtained from the advection-diffusion equation (2.15),

$$-w_s\frac{\partial C}{\partial y} = \frac{\nu}{Sc}\frac{\partial^2 C}{\partial y^2} \tag{5.5}$$

When supposing $C = 1.0$ at the bottom wall and $C = 0.0$ at the top wall, following vertical profile of the volumetric concentration is achieved,

$$C\left(y\right) = 1 + \frac{1 - e^{\frac{-w_s Sc}{\nu}y}}{e^{\frac{-w_s Sc}{\nu}2h} - 1} \tag{5.6}$$

Figure (5.1) illustrates vertical profiles of the mean streamwise velocity for the laminar close channel flow using the DNS and analytic solution. Averaging is done over horizontal planes and in time.

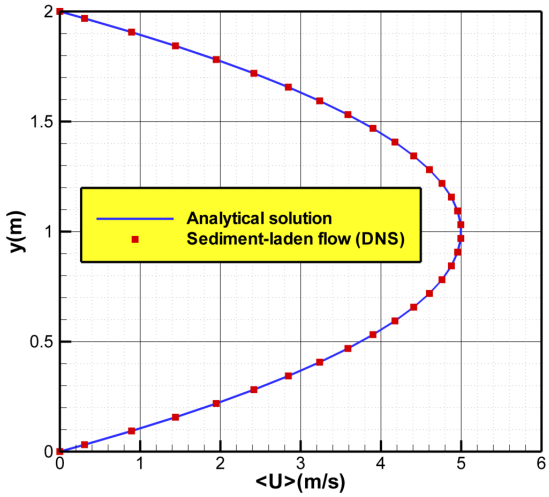

Figure 5.1 – Comparison between DNS and analytic solution in terms of the mean streamwise velocity

When the concentration profile manifested by equation (5.6) is introduced into the clear fluid, no change in the mean streamwise velocity is seen as expected.

Figure (5.2) demonstrates that there is an exact similarity between the analytic solution and DNS when evaluating the depth-averaged volumetric concentration.

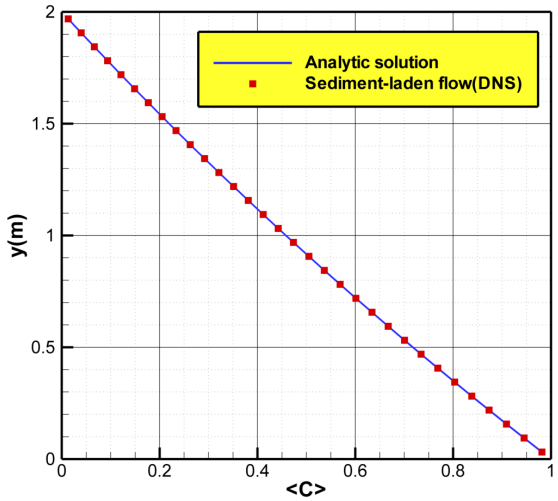

Figure 5.2 – Comparison between the DNS and analytic solution in terms of the mean volumetric concentration

5.2 Experimental data in literature

Muste et al. [2005] and Muste et al. [2009] researched experimentally the dilute dispersion of suspended sediment particles in a highly turbulent open channel flow by means of the particle image velocimetry (PIV) and particle-tracking velocimetry (PTV) techniques. The aim was to understand how suspended sediment affected flow structures and turbulence. The results were illustrated in terms of streamwise and vertical velocities, Reynolds stresses, turbulence intensities and volumetric concentration. The volumetric concentration of sediment particles was generally small and hence collisions between particles were negligible. All sediment particles were kept suspended and there was no deposition on the channel bed due to the imposed mass flow rate. The experimental flume was $6m$ long and $0.15m$ wide with water depth $h = 0.021m$. All measurements were conducted along the centerline of the flume, in a section positioned $5.3m$ from the entrance. The bed was made of smooth stainless steel and sidewalls were of the glass. From an experimental viewpoint, a flow-conditioning honeycomb structure was used at the entrance of experimental flume to facilitate the development of the flow turbulence. The sediment-laden flow was created by adding sand particles to the clear water flow. The slope of the channel was set at 0.0113 in all experiments. Flow uniformity was also ensured. Due to the large aspect ratio $AR = 7.5$, no effective secondary flows were reported. Faint

streaks were seen for the sediment-laden flow called NS3 where the bulk flow velocity was diminished 20 percent. The water surface waviness was $2-3mm$. Experimental conditions and pertinent flow variables in the single-phase mixture are shown in table (5.1).
Muste et al. [2005] called experiments with the natural sand as NS1, NS2 and NS3 corresponding to three separate volumetric concentrations, $C = 0.00046$, $C = 0.00092$ and $C = 0.00162$, respectively. As the volumetric concentration was increased, the deviation of the streamwise velocity in the sediment-laden flow from that in the clear water flow got bigger.
Subsequently, the experiment NS3 is used in present thesis to better explain interactions between turbulence and suspended sand particles.

Table 5.1 – Properties of the mixture flow in [Muste et al., 2005]

	Clear water	Sediment-laden flow (NS3)
Specific gravity s	-	2.65
Diameter $d(m)$	-	0.00023
Settling velocity $w_s(\frac{m}{s})$	-	0.024
Volum. concentration C	-	0.00162
Reynolds number Re	17670	17340
Froude number Fr	1.89	1.75
Shear velocity $u_*(\frac{m}{s})$	0.042	0.043
Bulk velocity $\tilde{U}(\frac{m}{s})$	0.839	0.792
von Karman κ	0.402	0.367
Temperature $\mathbf{T}(^0C)$	23	23

The sediment particles were the natural sand with $d = 0.23mm$. The settling velocity w_s was estimated from the empirical formulation proposed by Dietrich [1982]. It took into account effects of size, density, shape, and roundness.
The bulk Reynolds number Re and Froude number Fr are computed from,

$$Re = \frac{4R_h\tilde{U}}{\nu_m}, Fr = \frac{\tilde{U}}{\sqrt{gh}} \tag{5.7}$$

R_h and ν_m are the hydraulic radius and kinematic viscosity of the mixture, respectively.
As categorized by Muste et al. [2005], the shear velocity u_* for open channel flows could be computed from two methods, (1) momentum balance equation and (2) computed Reynolds stresses. From an experimental point of view, uncertainties are larger in the first method, hence the extrapolation of the Reynolds stresses was adopted.
High ratio between the shear velocity and settling velocity indicated that in this highly turbulent flow all sand particles are suspended. The insertion of sediment particles did not affect the bottom shear stress. Shear velocity were identical for

both clear water and sediment-laden flows. The kinematic viscosity was altered less than 0.9 percent when sediments were introduced into the clear water flow. So, $\nu_m \approx \nu$. The bulk flow velocity $\tilde{U}$ for the sediment-laden flow was lesser than that for the clear water and hence, the particle suspension extracted the energy from the flow and the turbulence was attenuated.
The von Karman constant κ was diminished with the addition of sediment particles meaning inside the inner region, there was a strong particle flow turbulence. Close to the bottom wall, the base fluid was bound by the viscous shear and particles were not. As a result, close to the channel bed, the streamwise velocity for the mixture was higher than that for the clear water.
Finally, no clear trend between the reduction of the von Karman constant and density variations demonstrated. The linear trend of the Reynolds stress was also preserved for the sediment-laden flow.

5.3 Simulation details

The two-phase coupled equations in the FEM framework [Ferry and Balachandar, 2001] are considered. Wall-resolving LES in the LES-COAST code is implemented to solve equations. It elucidates interactions between suspended sand particles and turbulence in experiments of Muste et al. [2005].
The effects of the viscous dissipation and gravity are totally insignificant. Preferential accumulation, turbophoresis or clogging of cohesive sediment particles are disregarded.
The dimensions of the computational domain are $2 \times \pi \times 0.021m$, $0.021m$ and $\pi \times 0.021m$ in the streamwise x, vertical y and spanwise z directions, respectively. The number of cells in x,y and z directions are 136, 128 and 192, respectively. According to mesh requirements in the wall-resolving LES, grids in x and z directions are homogeneous with $\Delta x^+ = 40.0$ and $\Delta z^+ = 14.0$. The grid in the vertical direction is stretched so that the first centroid is located at $y_1^+ = 0.5$ and nine cells are embedded below $y^+ = 10.0$. The grid requirement in the vertical direction is depicted in figure (5.3).
The periodic boundary condition for all key variables is imposed in x and z directions. A free-slip boundary condition is imposed at the top surface. No-slip boundary condition is defined at the channel bed. The Courant number is 0.5 and corresponding time step is $\Delta t = 3.917 \times 10^{-6} s$. Both molecular and turbulent Schmidt numbers, Sc and Sc_t, are unity in the numerical simulation. The dynamic eddy viscosity and diffusivity models are used to treat the SGS stresses and sediment fluxes.
Firstly, statistics of the turbulent flow of the clear water are gathered by imposing a constant mass flow rate. After that, a Rouse-fitted profile of the sediment concentration relating to the experiment NS3 of Muste et al. [2005] is introduced to the clear water flow.
More importantly, to ensure a fully-developed state for clear water and sediment-laden flows, instantaneous streamwise velocities at four different points in the vertical direction are checked.

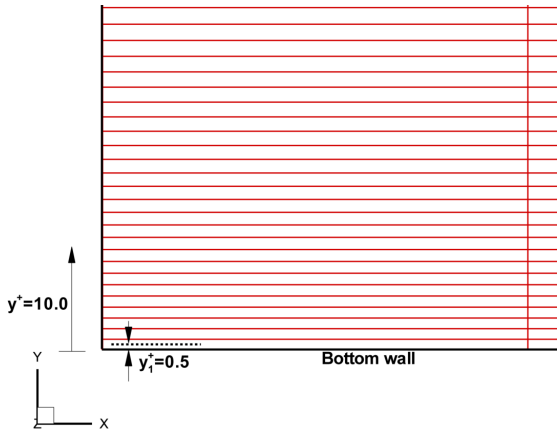

Figure 5.3 – Grid refinement in the vertical direction in the wall-resolving LES

5.4 Validations and findings

Figure (5.4) shows comparisons of the dimensionless streamwise velocity of the clear water flow between the present wall-resolving LES, theoretical study of Nezu and Nakagawa [1993] and experiment of Muste et al. [2005].

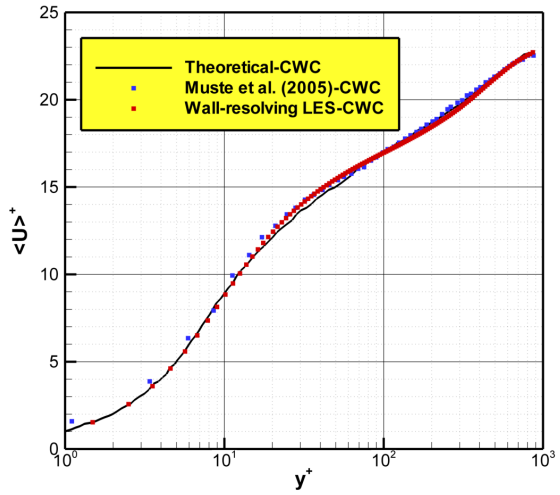

Figure 5.4 – Dimensionless depth-resolved streamwise velocity for the clear water flow against experimental [Muste et al., 2005] and theoretical [Nezu and Nakagawa, 1993] studies

Nezu and Nakagawa [1993] presented the log-law velocity distribution using

$\kappa = 0.41$ and $B = 5.5$. It must be highlighted that U, V and W are the averaged velocities in time. Symbol $\langle\rangle$ indicates averaging over horizontal planes. The streamwise velocity is made dimensionless using the shear velocity which is $0.042m/s$ in the wall-resolving LES. Shear velocity is computed at the first centroid off the bottom wall. It is located in the viscous sub-layer region where there is $\langle U\rangle^+ = y^+$. As would be seen, a satisfactory agreement is achieved regarding the dimensionless depth-resolved streamwise velocity for the clear water flow. Figure (5.5) manifests discrepancies between results of the wall-resolving LES and Muste et al. [2005] in terms of the depth-resolved vertical velocity for the clear water flow. A positive value means that the vertical velocity is directed upwardly to the free surface. Generally speaking, vertical velocities are too small compared to streamwise velocities. Largest downward depth-resolved vertical velocities are observed near the free surface complying with outcomes of Cellino [1998] and Graf and Cellino [2002]. It is found out in experiments that the depth-averaged vertical velocity was constant. It is much higher than that in the current wall-resolving LES. Reynolds shear stresses normalized with the shear velocity u_* for the clear water flow are compared in figure (5.6). Second-order statistics calculated here are the sum of corresponding resolved and SGS parts. The turbulent velocity fluctuations in streamwise and vertical directions are computed by,

$$u'(x,y,z,t) = u(x,y,z,t) - U(x,y,z) \tag{5.8}$$

$$v'(x,y,z,t) = v(x,y,z,t) - V(x,y,z) \tag{5.9}$$

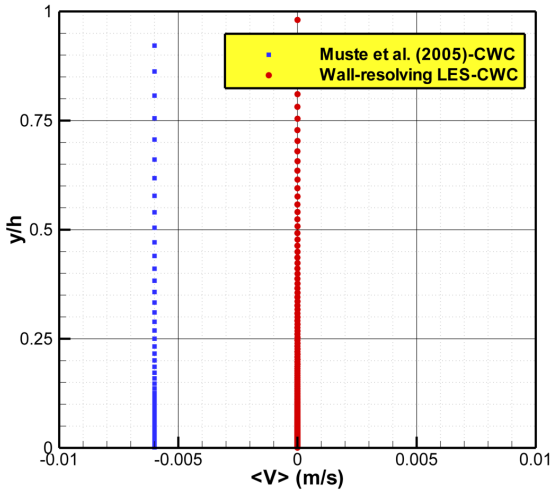

Figure 5.5 – Depth-resolved vertical velocity for the clear water flow against [Muste et al., 2005]

The linear variation of the Reynolds shear stress after some distance off the bottom wall demonstrates that flow is fully developed. The streamwise turbulence

intensities for the clear water flow are illustrated in figure (5.7). The RMS is computed from,

$$u_{rms} = \sqrt{\langle u'u' \rangle}, v_{rms} = \sqrt{\langle v'v' \rangle} \tag{5.10}$$

The streamwise turbulence intensity is the RMS of the streamwise turbulent velocity fluctuation normalized by the shear velocity.

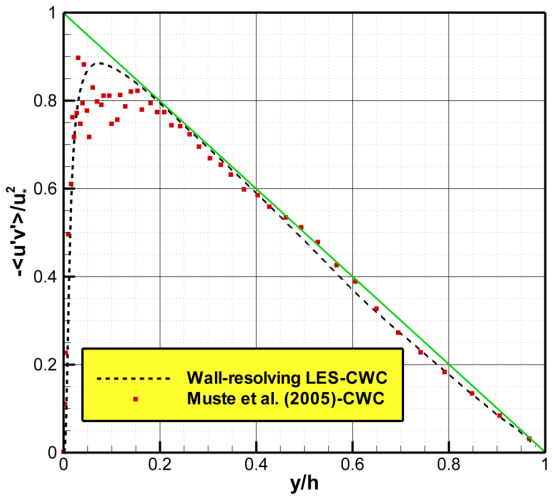

Figure 5.6 – Depth-resolved Reynolds stress for the clear water flow against Muste et al. [2005]

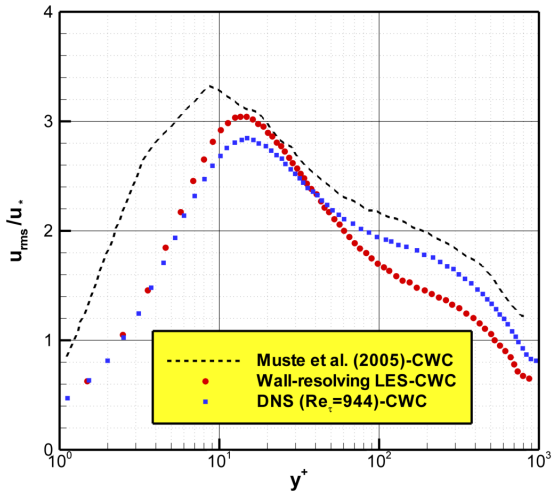

Figure 5.7 – Streamwise turbulence intensity for the clear water flow against DNS data [Hoyas and Jimenez, 2008] and experiment of Muste et al. [2005]

The comparison is fulfilled against experimental data [Muste et al., 2005] and DNS database of a close turbulent channel flow at turbulent Reynolds number $Re_\tau = 944$. This DNS was provided by Hoyas and Jimenez [2008]. The turbulent Reynolds number in the present wall-resolving LES of the clear water flow is $Re_\tau = 882$. As could be comprehended, the streamwise turbulence intensity in experiment [Muste et al., 2005] is much bigger than those in the wall-resolving LES and DNS. Even the DNS with a higher Re_τ gives a lower level of fluctuations with respect to experiments. It is worthy to mention that the underestimation of the streamwise turbulence intensity was also recorded by Chauchat and Guillou [2008]. They validated experimental data using a 2D two-phase formulation with $k - \epsilon$ closure model. k is the turbulent kinetic energy. More specifically, the maximum of the streamwise turbulence intensity in the DNS and wall-resolving LES is equal to 2.82 and 3.0, respectively. In experiments, it is 3.3. Furthermore, the apex of the streamwise turbulence intensity in experiments is well below $y^+ = 10$. However, the maximum of the streamwise turbulence intensity was at $y^+ = 14$ [Chauchat and Guillou, 2008], $y^+ = 15$ [Hoyas and Jimenez, 2008] or $y^+ = 17$ [Nezu and Rodi, 1986]. In figure (5.8), the vertical turbulence intensity for the clear water flow is compared against existing DNS and experiments.

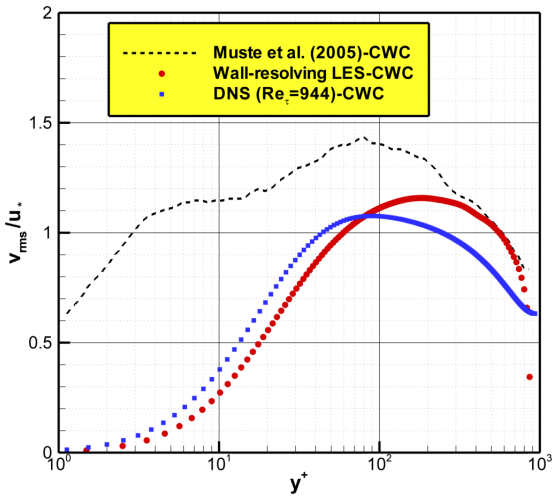

Figure 5.8 – Vertical turbulence intensity for the clear water flow against DNS [Hoyas and Jimenez, 2008] and experiment of Muste et al. [2005]

Again, DNS and wall-resolving LES highly underestimate the vertical turbulence intensity obtained in experiment of Muste et al. [2005] except near the free surface. Close to the free surface, vertical turbulence intensities from the wall-resolving LES and experiment are same. On contrary, Chauchat and Guillou [2008] reported the overestimation of the vertical turbulence intensity with the friction velocity $u_* = 0.047m/s$ using a 2D $k - \epsilon$ numerical model.

Like the numerical study of Chauchat and Guillou [2008], the profile of the sediment concentration in the experiment NS3, which is demonstrated in figure (5.9), is imposed to the fully developed clear water flow.
The maximum of the volumetric sediment concentration is above the channel bed. The experimental profile of the sediment concentration was matched by a Rouse-fitted profile,

$$Rn = \frac{w_s}{\beta \kappa u_*} = 0.19, \beta = \frac{1}{Sc_t} = 0.22 \tag{5.11}$$

Rn is the fitted Rouse number. β is the inverse of the turbulent Schmidt number. Kundu and Ghoshal [2014] theoretically categorized relationships between the direction of vertical velocities induced by secondary currents and the shape of the concentration profile.

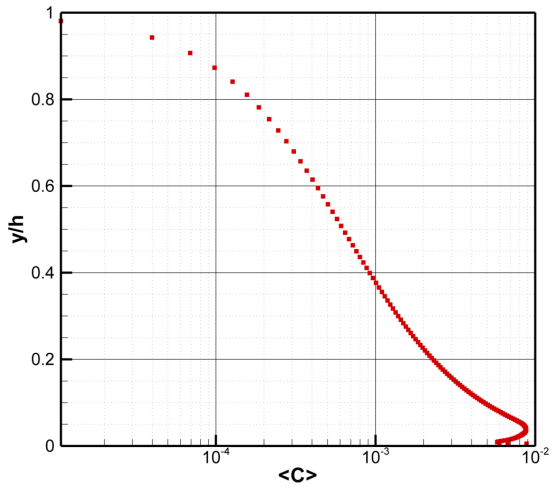

Figure 5.9 – Imposed profile of the sediment concentration from experiment NS3 of Muste et al. [2005]

In type (I), the maximum of the sediment concentration is on the channel bed and the vertical velocity is downward. In type (II), the maximum is at some distance off the bottom wall. It is seen in figure (5.9). Vertical velocity is upward. In contrast to explications of Kundu and Ghoshal [2014], Muste et al. [2005] recorded negative vertical velocities and absence of any secondary currents while the concentration profile for experiment NS3 was acquired. Yu et al. [2014] presented figure (5.10) for clarifying better results of experiment NS3. When sediment particles are introduced to the flow, the streamwise velocity of the mixture is decelerated inside the outer region. It is due to the velocity lag between particles and water. On the other hand, the streamwise velocity of the mixture is expedited within the inner region because sediment particles without viscosity move faster than water. The gradient of the streamwise velocity

distribution gets steeper inside the buffer layer near the bed. Accordingly, the von Karman constant declines.

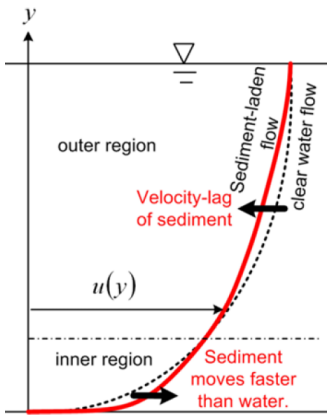

Figure 5.10 – How suspdended sediment particles modify the streamwise velocity, taken with courtesy from [Yu et al., 2014]

Figure (5.11) shows influences of suspended natural sand particles on the dimensionless depth-resolved streamwise velocity in a highly turbulent open channel flow. Once sediment particles are in the flow, the bulk flow velocity $\tilde{U}$ is reduced from $0.839m/s$ to $0.799m/s$ in the wall-resolving LES. Error is less than one percent compared to $\tilde{U} = 0.792m/s$ in the experiment NS3.

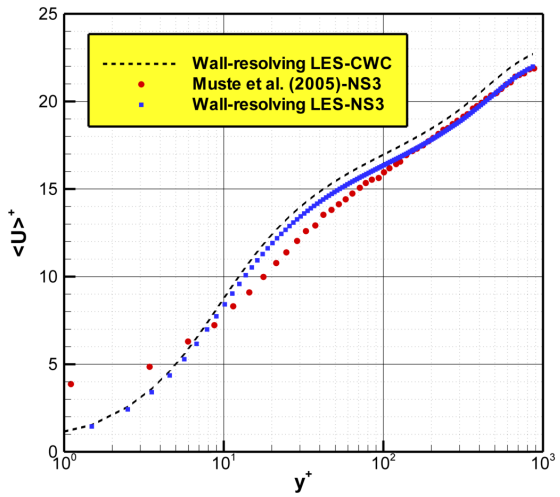

Figure 5.11 – Effect of imposed profile of the sediment concentration in the experiment NS3 on the dimensioneless depth-resolved streamwise velocity

Besides, for clear water and sediment-laden flows, the friction velocity is $u_* =$

$0.042m/s$ and $u_* = 0.041m/s$, respectively. Contrary to Yu et al. [2014] and Muste et al. [2005], in the wall-resolving LES, no acceleration of the depth-resolved streamwise velocity inside the inner region is seen when sediment particles are introduced. It substantiates that the friction velocities for clear water and sediment-laden flows are same. Also inside the outer region, the depth-resolved streamwise velocity is abated for the sediment-laden flow. Suspending sand particles reduces the drag force. Similar to conclusions of Muste et al. [2005], imposing the buoyancy term g_m does not have any effect on the depth-resolved streamwise velocity. There is no influence of suspended sediment particles on the Reynolds stresses.

Chapter 6

Case study II: unresolved wall function LES of SST

6.1 Experimental data in literature

Cellino [1998] and Graf and Cellino [2002] performed experimental studies on the SST in a recirculating tilting open channel flow with bottom rough wall. The length and width of the channel were $16.8m$ and $0.6m$, respectively. To measure data, a section was chosen $13m$ from the entrance of the channel where the boundary layer established. Measurements were performed by a sonar instrument (Acoustic Particle Flux Profiler, APFP) which was located at the center-line of this cross section. The imposed flow discharge, which was continuously checked using a magnetic flowmeter, provided $h = 0.12m$. Graf and Cellino [2002] emphasized that the aspect ratio (AR) of the channel was big enough to consider the flow bidimensional. Channel bed was rough but infiltration of sediments on that was totally prevented. The mixture flow was steady and uniform. It was in the capacity condition meaning a sediment layer with a constant thickness of $2mm$ covered the bottom rough wall. Remaining sediments were in the suspension mode. Bed slope was equal to the channel slope. The sediment particles were of non-cohesive natural sand with,

$$d = 0.135mm, s = 2.65, w_s = 0.012\frac{m}{s} \tag{6.1}$$

Table (6.1) presents pertinent variables for the clear water and sediment-laden flows in experiments of Cellino [1998].
The APFP instrument provided the instantaneous vertical profiles of longitudinal (streamwise) $u(y,t)$ and vertical $v(y,t)$ velocities. In the experiment of Cellino [1998], the bulk velocity was computed from,

$$\tilde{U} = \frac{1}{h}\int_0^h U(y)dy \tag{6.2}$$

Note that $U(y)$ is the average streamwise velocity in time. Shear velocity u_* can be approximated using the energy-gradient method or Reynolds-stress method. The extrapolation of the Reynolds stresses towards the channel bed gives the shear velocity.

Table 6.1 – Germane variables in experiments of [Cellino, 1998]

	CW_S015	SLF (Q40S003)
Discharge $Q(\frac{m^3}{s})$	0.05	0.049
Flow depth $h(m)$	0.12	0.12
Aspect ratio AR	5.0	5.0
Bed slope $S_b(\%)$	0.15	0.03
Bulk velocity $\tilde{U}(\frac{m}{s})$	0.726	0.68
Reynolds number Re	248900	233000
Froude number Fr	0.67	0.63
Friction velocity $u_*(\frac{m}{s})$	0.045	0.028
Friction factor f	0.031	0.014
Equivalent roughness $k_s(m)$	0.0012	0.00005
Dimensionless roughness k_s^+	54.0	1.4
Particle diameter $d_{50}(m)$	-	0.000135
Sediment density $\rho_s(\frac{kg}{m^3})$	-	2650
Settling velocity $w_s(\frac{m}{s})$	-	0.00012
Volum. concentration C	-	0.00077
Density $\rho_m(\frac{kg}{m^3})$	1000.0	1001.28
Kinematic viscosity $\nu_m(\frac{m^2}{s})$	0.000001	0.000001002
von Karman κ	0.4	0.4

In agreement with Coleman [1981], the von Karman constant was $\kappa = 0.4$ for clear water and sediment-laden flows. The friction factor f is estimated by,

$$f = 8\left(\frac{u_*}{\tilde{U}}\right)^2 \tag{6.3}$$

The equivalent bed roughness k_s is given by the phenomenological Colebrook-White equation,

$$\sqrt{\frac{1}{f}} = -2.log\left(\frac{k_s}{a_f R_h} + \frac{b_f}{Re\sqrt{f}}\right) \tag{6.4}$$

The constants a_f and b_f are equal to 11.5 and 3.0, respectively. In order to specify the type of turbulent flows, the roughness height in the dimensionless form is calculated,

$$k_s^+ = \frac{k_s u_*}{\nu_m} \tag{6.5}$$

k_s^+ is called the roughness Reynolds number in experiments of Cellino [1998]. If it is lower than 5.0, the bed is considered hydraulically smooth and the constant of the integration in the log-law equation (3.36) is $B = 5.5$. If it is between 5.0 and 70.0, the bed is hydraulically in the transitional condition. For $k_s^+ > 70.0$, the bed is hydraulically rough with $B = 8.5$. As Cellino [1998] showed, the classical log-law in transitional and fully rough turbulent open channel flows is,

$$\frac{U}{u_*} = \frac{1}{\kappa} \ln\left(\frac{y}{k_s}\right) + B \tag{6.6}$$

Appropriate length-scale in hydraulically smooth open channel flow is the viscous length-scale [Pope, 2000]. In transitional and fully rough ones, it is equivalent to the bed roughness k_s. In experiments, for the clear water flow, k_s^+ is 54.0 and hence, the channel bed is hydraulically transitional. For the sediment-laden flow (Q40S003), it is 1.4 so the bed is hydraulically smooth. While the mixture density is taken from equations (2.23) and (2.24), the kinematic viscosity ν_m is modified using [Cellino, 1998],

$$\nu_m = \nu \times \frac{\rho_0 \left(1 + 2.5C\right)}{\rho_0 + \left(\rho_s - \rho_0\right) C} \tag{6.7}$$

Kinematic viscosity is changed around 0.2 % so physical conclusions are not related to the viscosity change. Cellino [1998] stated that clear water formulations still can give a reasonable and theoretical-empirical description of the suspension flow if the volumetric concentration is small $C < 0.01$, size of particles is so tiny, sediments are not cohesive and Newtonian rheological law is valid. If sediment particles are too smaller than the micro-scale of the turbulence λ, they may follow smallest eddies in the flow.

6.2 Simulation details

In the LES-COAST code, the single-phase Euler-Euler based unresolved wall function LES with the equilibrium stress model is selected to analyze interactions between suspended sediment particles and turbulence. Results are compared against experiments of Cellino [1998]. In the numerical simulation, channel dimensions in x, y and z directions are $2 \times \pi \times 0.12m$, $0.12m$ and $\pi \times 0.12m$, respectively. Number of cells is $32 \times 32 \times 32$. Both the molecular and turbulent Schmidt numbers, Sc and Sc_t are 1.0. For the SLF and CWC, the constant in Smagorinsky model is $C_s = 0.065$. The Courant number in this study is 0.2. Time step (Δt) changes over time around $2 \times 10^{-3} s$ to get a fixed Courant number. The flow is driven by imposing a constant pressure gradient divided by the water density and it is equal to 0.021 and 0.0081 for the CWC and SLF, respectively. It is found that the wall shear stress on the sidewalls should be included in the calculation of the imposed pressure gradient. According to Yang et al. [2012], the shear stress on each sidewall is equal to $0.63 \times \tau_w$. τ_w is the bottom shear stress obtained from the energy-gradient method. The same

roughness as expressed in experiments is applied differently for the CWC and SLF. In addition, no-flux condition for the sediment concentration is defined at the free surface. Periodic boundary condition is defined in the streamwise and spanwise directions. The initial state of the open channel flow is obtained by interpolating from a highly turbulent closed channel flow. After reaching the steady state, statistics of the CWC are gathered. Then, a constant profile of the sediment volumetric concentration $C = 0.000773$ is imposed to get statistics of the SLF. The reference concentration formulation proposed by Smith and Mclean [1977] together with the Shields diagram is used to treat the erosion of sediment particles from the channel bed. It is supposed that the buoyancy induced by suspended sediment particles could affect hydrodynamics of the flow and hence the two-way coupling is applied. Modified gravity term derived by Winterwerp [2001] in the Navier-Stokes equations of the SLF is introduced.

6.3 Validations and findings

Figure (6.1) demonstrates influences of suspended sediment particles on the streamwise velocity. Table (6.2) presents the bulk velocity, friction velocity and position of the first centroid off the bottom wall. They are obtained from the unresolved wall-function LES. The friction velocity is obtained from the extrapolation of the Reynolds stress inside the upper layer.

Table 6.2 – Key variables obtained from the unresolved wall-function LES

	CW_S015	SLF (Q40S003)
Bulk velocity $\tilde{U}(\frac{m}{s})$	0.73	0.69
Friction velocity $u_*(\frac{m}{s})$	0.049	0.03
Position of first centroid y_1^+	91.87	56.25

When comparing the bulk velocity from the unresolved wall function LES to that in experiments, it is found that the error is around 2 percent.
Compared to the CWC, it is seen that the suspension of sand particles engenders the reduction of the friction velocity and roughness. From a theoretical point of view, inside the inner region $y < 0.2 \times h$ the universal law-of-the-wall (log-law) and inside the outer region $y > 0.2 \times h$ law-of-the-wake (Cole's law) could be applied to get the streamwise velocity of the flow over smooth and rough beds. As could be observed from experimental data in figure (6.1), the maximum of the streamwise velocity was not at the free surface. Yang et al. [2004] theoretically proved that secondary currents induced the non-zero mean vertical velocity and the deviation of the Reynolds shear stress from the conventional linear distribution. Furthermore, the maximum streamwise velocity occurs below the free surface. Yan et al. [2011] mentioned that for narrow open channels ($AR \leq 5.0$), the flow becomes actually 3D. Toorman [2003] hypothesized that deviations

from the logarithmic law close to the free surface in experiment of Cellino [1998] were probably created by secondary currents and friction with the sidewalls.

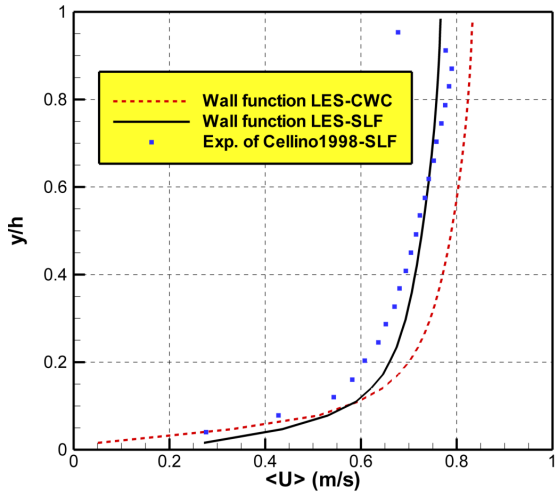

Figure 6.1 – Comparison of the streamwise velocity against experiments of Cellino [1998]

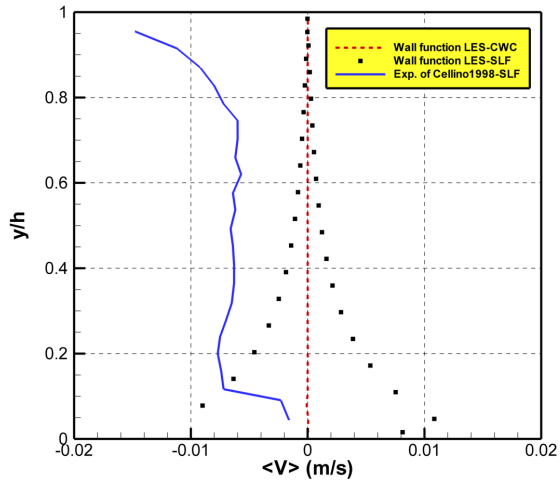

Figure 6.2 – Comparison of the vertical velocity against experiments of Cellino [1998]

More importantly, as is seen in the experiment of Cellino [1998], suspending sand particles in the flow results in the decrease of the bulk velocity like Muste et al. [2005]. More specifically, in accordance with conclusions of Muste et al.

[2005], the streamwise velocity is reduced inside the outer layer. Flow is accelerated in the super-saturated region close to the bottom wall because there are high inter-particle collisions between sediment particles which are not bounded by viscosity.
Figure (6.2) demonstrates effects of suspended sediments on the vertical velocity. A positive value means the velocity is directed upward to the free surface. Generally speaking, vertical velocities are too small in comparison with streamwise velocities. In experiments of Cellino [1998], largest downward vertical velocities were recorded near the free surface. Secondary flows created non-zero vertical velocities based on Yang et al. [2004]. Unresolved wall-function LES shows that vertical velocities for the sediment-laden flow in lower levels are significantly higher than vertical velocities for the clear water flow. Close to the free surface, vertical velocities for clear water and sediment-laden flows are equal.

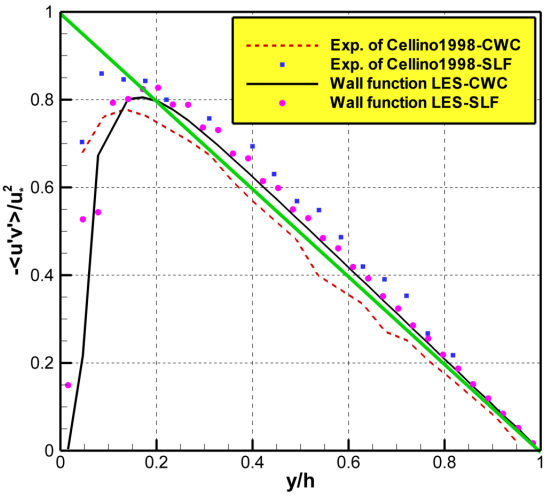

Figure 6.3 – Comparison of the Reynolds shear stress against experiments of Cellino [1998]

The Reynolds stresses obtained from experiments and unresolved wall-function LES for the CWC and SLF are shown in figure (6.3).
Pay attention that in the viscous sub-layer region, the Reynolds shear stress is negligible compared to the viscous stress. For $y > 0.05 \times h$, the total shear stress may be well approximated by the Reynolds shear stress. The linear variation of the Reynolds shear stress after some distance from the bottom wall indicates that there is uniform flow. Analogous to Cellino [1998], the Reynolds stress deviates from the linear trend inside the inner region $y < 0.2 \times h$. Erosion and deposition take place in this region and the sediment concentration is high.
The streamwise turbulence intensity from the unresolved wall-function LES is compared against experimental data of Cellino [1998] and Kironoto [1992] in figure (6.4). Kironoto [1992] experimentally reported that for the uniform open

channel flow of the clear water over a rough bed, streamwise and vertical turbulence intensities are estimated by,

$$\frac{u_{rms}}{u_*} = 2.04 \times e^{\left(-0.97 \times \frac{y}{h}\right)} \tag{6.8}$$

$$n\frac{u_{rms}}{u_*} = 1.14 \times e^{\left(-0.76 \times \frac{y}{h}\right)} \tag{6.9}$$

Kironoto [1992] showed distributions of turbulence intensities by the universal exponential law. 2D flow variables in experiments of Kironoto [1992] and Cellino [1998] are comparable. Cellino [1998] illustrated that inside the inner region $y < 0.2 \times h$, the presence of sand particles induced the intensification of the streamwise turbulence intensity. Within the outer region $y > 0.2 \times h$, there is no detectable difference between the CWC and SLF. This is what Muste et al. [2005] also reported.

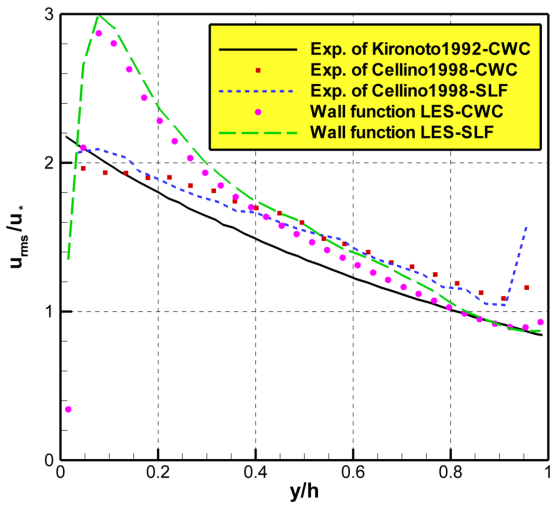

Figure 6.4 – Comparison of the streamwise turbulence intensity against experiments of Cellino [1998] and Kironoto [1992]

Inside the outer region, data of Cellino [1998] totally overestimates the streamwise turbulence intensity obtained from experimental correlation of Kironoto [1992]. Regarding the unresolved wall function LES, it is seen that the streamwise turbulence intensity for the sediment-laden flow is bigger than that for the clear water case. Close to the free surface they are identical to data of Kironoto [1992] and Cellino [1998]. This similarity is due to noticeable decrease of the sediment concentration near the free surface.
The vertical turbulence intensity from the unresolved wall-function LES is compared against experimental data of Cellino [1998] and Kironoto [1992] in figure (6.5).

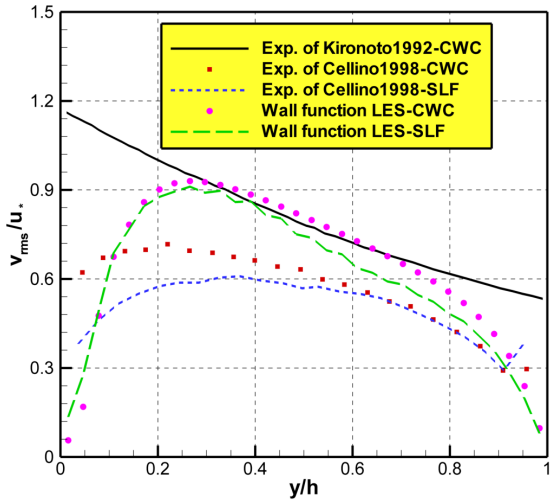

Figure 6.5 – Comparison of the vertical turbulence intensity against experiments of Cellino [1998] and Kironoto [1992]

As Cellino [1998] found out, suspending sand particles in the clear water flow caused the attenuation of the turbulence more remarkably close to the bed. It is seen from the unresolved wall-function LES that near the bed, the presence of suspended sand particles results in the slight enhancement of the vertical turbulence intensity. In upper levels, significant weakening of the vertical turbulence intensity is seen. Adjacent to the free surface, vertical turbulence intensities for the CWC and SLF are identical since the sediment concentration is low. In contrast to Cellino [1998], a better convergence in the middle of the channel is achieved using the unresolved wall-function LES against results of Kironoto [1992]. In figure (6.6), the sediment concentration from the unresolved wall-function LES is compared against experimental data of Cellino [1998]. The experimental variation of the sediment concentration was matched by a Rouse-fitted profile like,

$$Rn = \frac{w_s}{\beta \kappa u_*} = 2.15, \beta = \frac{1}{Sc_t} = 0.498, C_{ref} = 0.00929 \tag{6.10}$$

When the buoyancy term is deactivated, the sediment concentration is high and unsatisfactory higher-order turbulence statistics are gathered with the unresolved wall-function LES. Analogous to the study of Toorman [2003], experimental results are underestimated close to the free surface. In experiments, the streamwise velocity was deviated from the logarithmic profile due to the existence of secondary currents. Near the free surface, large velocity gradients produced more turbulence and kept more sediments in the suspension mode compared to the theory of Toorman [2003] for infinitely wide channels. From an experimental viewpoint, the accuracy of very low values of the concentration near the free surface is highly questionable. Understanding of highly saturated

layer of the sediment close to the bed is done only qualitatively [Toorman, 2003].

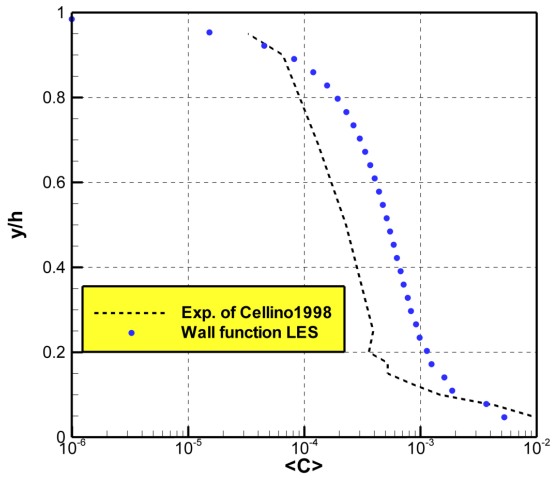

Figure 6.6 – Comparison of the sediment concentration against experiments of Cellino [1998]

Chapter 7

Propagation of suspended sediment wave in macro-rough flow

7.1 Literature review on macro-rough flow

Channelized rivers from a geometrical point of view are simple configurations because they have a straight path. In natural morphology, however, a high diversity across the channel bed or bank may be seen. In river restoration applications, hydraulics engineers artificially alter the natural path and geometry of rivers by creating lateral cavities. Lateral macro-roughness cavities are generated to improve the habitat diversity. The dead zone areas are refugees for fishes and are targets for spawning. They have implications for the sediment management in rivers and propagation of contaminants. Large-scale irregularities may change the SST in rivers. Macro-rough boundaries could influence the propagation of a suspended sediment wave in a turbulent open channel flow.
Bathurst [1985] defined if ratio between flow depth (h) and characteristic size of the roughness element (k) was less than 4, flow was a macro-rough one. According to Meile [2007] and Meile et al. [2011], when the size of lateral roughness elements was comparable to the flow depth or hydraulic radius of the channel, there was a macro-rough flow. Lyapin [1994] found out experimentally that canals with increased bottom roughness were those in which the ratio between h and k was lower than 5. These macro-roughness elements could be mounted laterally or on the bottom surface. The macro-roughness elements may cover entire channel section or only a part of it so arrangement is important.
Considering lateral macro-rough flows, Meile [2007] stated that longitudinal waves were created in the streamwise direction (x) while the transversal waves were oscillated in the crosswise direction (z). By increasing the flow depth, the effect of the bank roughness got more prominent. The cavity flows, which

are generated by lateral macro-roughness elements, are frequently examined in terms of their trapping efficiency and corresponding aspect ratio.
When the cavity aspect ratio ϑ_{cf} is between 0.15 and 0.6, a primary vortex and a secondary vortex with a much lower velocity are detected. For $\vartheta_{cf} = 0.8$, a single circular vortex is seen inside the cavity flow. Meile [2007] and Meile et al. [2011] recorded the existence of unstable recirculation zones, wake regions, coherent structures, mixing layers and oscillations of the flow in the transverse direction (z). As prescribed in the literature, for the bottom roughness, the more the velocity or water depth augments, the more the influence of roughness elements abates. Ashrafian and Andersson [2006] concluded that mounting of roughness elements on the bottom wall resulted in the reduction of the size of large-scale flow structures within the roughness sub-layer using flow visualization techniques. Moreover, extra eddies were generated that led to the consumption of the mechanical energy and an elevated resistance to the flow. Ashrafian et al. [2004] characterized this roughness sub-layer as a non-equilibrium shear layer in which sturdy inhomogeneities, particularly close to roughness elements were observed. Tachie et al. [2000] hypothesized that the presence of the wall roughness might be a source of secondary flows. It was resulted in the damping of vertical fluctuations of the velocity under the free surface. The decrease of the vertical velocity of the flow was another consequence. Correspondingly, the flow below the free surface could be retarded and the maximum streamwise velocity was seen some distance below the free surface. It is obvious that the influence of the roughness of the bottom wall could be comprehended well further than roughness sub-layer. As a result, the wall-similarity hypothesis [Bisceglia et al., 2001], fails to describe flows over bottom rough walls. It is known that the distribution and size of macro-rough elements existing on the bed have a more prevailing role than the viscous length scale on near-wall turbulent structures. To understand the hydraulic resistance and turbulent characteristics of bottom macro-rough turbulent flows in a simplified way, the homogeneous arrangement of bottom elements is considered in this study. Homogeneity [Romdhane et al., 2017] implies that crosswise strips have identical length as the channel width. Both d-type roughness [Djenidi et al., 1994] [Bisceglia et al., 2001] in which spacing is equal to the height of the roughness element and k-type roughness [Perry et al., 1969], in which spacing is bigger than the height of the roughness element, are investigated experimentally here.
The ratio ϑ of the distance w between bottom roughness elements and height of bottom roughness elements k is defined by,

$$\vartheta = \frac{w}{k} \tag{7.1}$$

The variable γ represents the ratio between the roughness height k and flow depth h,

$$\gamma = \frac{k}{h} \tag{7.2}$$

Leonardi et al. [2007] emphasized that with the d-type roughness, the frictional drag was much larger than the pressure drag. Lyapin [1994] did experimental

visualization of fluid flows over rough surfaces. It was confirmed that the appreciable space between bottom roughness elements was occupied by stagnant vortex zones. More specifically, for a d-type rough wall, because elements were closely spaced, stable vortices were formed within cavities, and no eddy shedding into the flow was above bottom elements. It was discovered by Romdhane et al. [2017] that the wall skin friction coefficient c_f in the d-type roughness type was identical to that in the smooth case. The flow visualizations for the square bar roughness [Djenidi et al., 1999] showed that near-wall structures called longitudinal streaks, which were observed the over smooth wall, were also seen over roughness elements. Jimenez [2004] specified that walls with grooves bigger than 3 or 4 times of the roughness height behaved like a k-type roughness. Extra form drag was generated and the viscous cycle was entirely destroyed. Meile [2007] reported that no streaky structures in the fully rough flow were present in case of the k-type roughness. Leonardi et al. [2004] performed the DNS of a fully turbulent channel flow with square bars with the height of $0.2 \times h$ on the bottom wall. Turbulent Reynolds number Re_τ ranged from 180 (smooth case) to 460 ($\vartheta = 7.0$). When the ratio ϑ was so small below 3, turbulence structures and intensities were like those in the smooth channel case. When the flow was driven by the imposed pressure gradient or constant mass flow rate, Leonardi et al. [2003] and Leonardi et al. [2004] observed numerically that the mean streamwise velocity in the d-type and k-type roughness cases was decreased compared to the smooth case. The maximum decrease was reported for the bottom rough case with $\vartheta = 7.0$ which showed the maximum form drag. Using the LES, Cui et al. [2003] ascertained that for the k-type roughness, the separation and reattachment took place between two consecutive bottom roughness elements and eddies were ejected into the outer flow.

Maechler [2016] highlighted experimentally relationships between the discharge, suspended sediment concentration and aspect ratio of cavities in a channel with lateral macro-roughness elements. The experimental channel represented a channelized river where artificial banks were adapted. Clear water flow was noticeably affected by the lateral embayments. It had been shown that the creation of the dead zones in the lateral macro-rough flows induced the deposition of suspended sediment particles. Deposition areas of sediment particles matched with the flow pattern analysis. Configuration with high discharge showed lowest decay of the sediment concentration due to enhanced flow turbulence and strong oscillations. Finally, preliminary tests on configurations showed that the flow was perturbed up to $3m$ from entrance and hence the deposition of sediments was affected. Moreover, the regulating downstream gate modified values shown by the turbidimeter. So, the probe 2 was shifted $1m$ to the upstream part.

Juez et al. [2017] analyzed influences of lateral macro-roughness elements on the transport of fine sediments in open channel flows. Banks were equipped with large-scale rectangular roughness elements. Influences of the flow shallowness and geometric ratios of cavities were discussed. Sheltered areas within cavities were identified by streamlines. They were areas where particles settled. The longer sediment particles remained inside the cavity, where the turbulence was weaker than in the main channel, the higher probability of the settling. For

highest discharge, small-scale fluctuations were homogenized, the vertical mixing promoted and sediment particles were hindered from the settling.
As could be seen, works relating to hydrodynamics and morphodynamics of lateral embayments in open channel flows are rare and complicated to perform. Sedimentation processes depend on the geometrical configuration of river banks. Also, effects of bottom macro-rough boundaries on the propagation of a suspended sediment wave in turbulent open channel flows should be elucidated. Turbulence and the decay of the suspended sediment concentration are related to spacing between bottom macro-rough elements.

7.2 Experimental setup

The hydraulic system consists of tanks in the upstream and downstream parts and rectangular flume. Dimensions are shown in table (7.1). Lateral macro-roughness configurations are built using the limestone bricks. Their dimensions are demonstrated in figure (7.1). Square wooden bars with the width of $1.75cm$, height of $1.75cm$ and length of $60cm$ are bottom macro-roughness elements. Figure (7.2) shows recirculating water pipes, two manually regulated pumps and two magnetic flow meter devices.

Table 7.1 – Dimensions of the flume and tanks in experiments

	Length(x)	Height(y)	Width(z)
Upstream tank	2m	1m	1m
Downstream tank	3.5m	1m	1m
Flume	7.5m	0.47m	1m

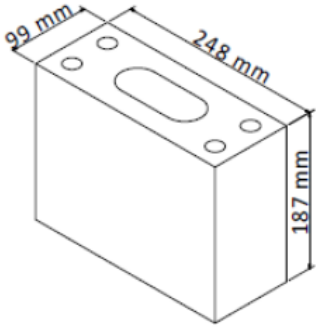

Figure 7.1 – Dimensions of limestone bricks

Figure (7.2b) depicts locations of outlets in the upstream tank. It engenders the enhancement of the mixing by inducing an upward flow.

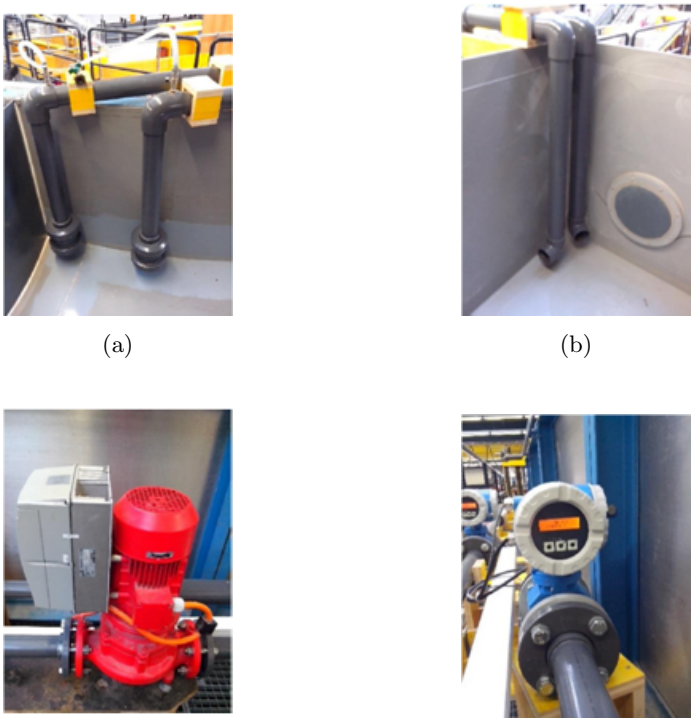

(a) (b)

(c) (d)

Figure 7.2 – Details of setup: downstream (a) and upstream (b) sections of the recirculating pumping system, manually regulated pump (c) and magnetic flow meter (d)

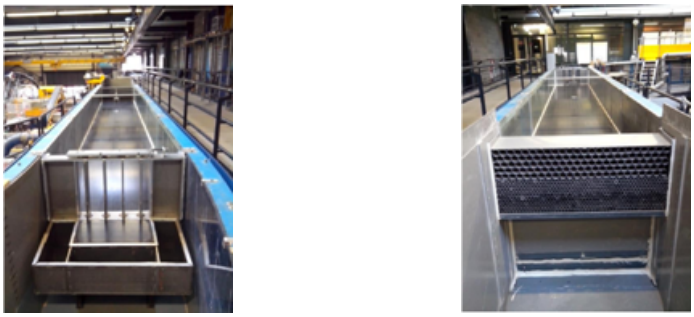

(a) (b)

Figure 7.3 – Details of setup: regulating mechanism in the downstream section (a) and tranquilizing structure in upstream section (b)

The maximum allowable mass flow rate in this hydraulic system is 18 liter per second to eradicate the cavitation. There is a pump inside the downstream tank making effectively the mixing of water and sediment.
To set the water height in the flume, a regulating mechanism consisting of the four rotating blades, which restricts the flow in the downstream part, is manufactured. Also, to direct appropriately the flow into the channel, a tranquilizing structure is mounted at the entrance. Both mechanism and structure are illustrated in figure (7.3).
The experimental flume in absence of any macro-roughness elements is exhibited in figure (7.3).
A slope of 0.1% is used for the experimental flume. Side and bottom walls are made of glass and Bakelite, respectively. There is a porous plate in figure (7.3a) in the downstream tank for collecting dirt from the hydraulic system.
To obtain the instantaneous sediment concentration, two turbidimeters COSMOS^R-25 are embedded vertically in the flow. The probe of turbidimeters (T_1 and T_2) is linked to a transmitter b-line multi amplifier by wires (Zullig AG, Switzerland).
To connect the probe to a computer, there is an acquisition card NI-USB-6259 M series (NI Instruments, USA) between transmitter and computer. All of these components are shown in figure (7.4).
Turbidimeter demonstrated in figure (7.4b) enables the measurement of a wide range of suspended solids from 0.001 to 400 gram per liter. The sensor in this device utilizes infrared beams transmitted and received to and from medium. Surface for the measurement of the concentration is planar and the sensor surface is flat and polished. This device could be used in open channel flows.

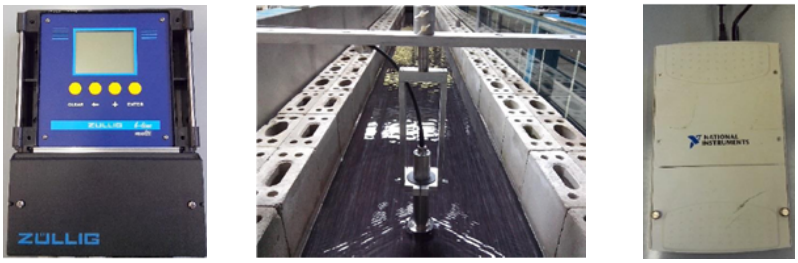

(a) (b) (c)

Figure 7.4 – Details of setup: transmitter b-line multi-amplifier (a), turbidimeter probe (b) and acquisition card NI-USB-6259 M series (c)

The diameter of the turbidimeter is equivalent to $0.04m$. Minimum distance of the bottom surface of the turbidimeter off the bottom wall must be $0.01m$ in order to eradicate erroneous reflections from the bed and high temporal concentration.
The card in figure (7.4c) is connected to a computer with the LABVIEW software installed on to visualize the temporal sediment concentration.

7.3 Configurations and procedure

Figure (7.5) demonstrates top-view sketches of the reference case (without any macro-roughness) and lateral macro-roughness banks under investigation in this study.

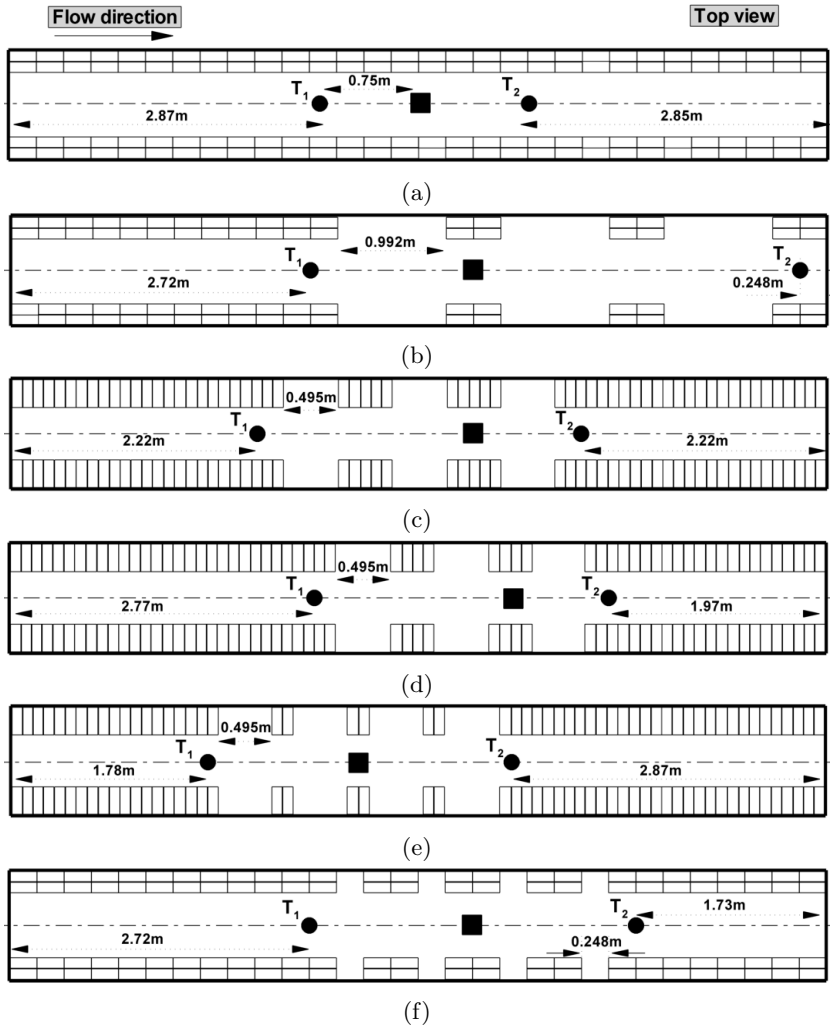

Figure 7.5 – Reference case (a) and lateral macro-roughness banks $L1$ (b), $L2$ (c), $L3$ (d), $L4$ (e) and $L5$ (f) - ● and ■ symbols representing positions of turbidimeters T_1 and T_2 and water height measuring device, respectively

Bottom macro-roughness configurations together with the reference case are shown in figure (7.6).

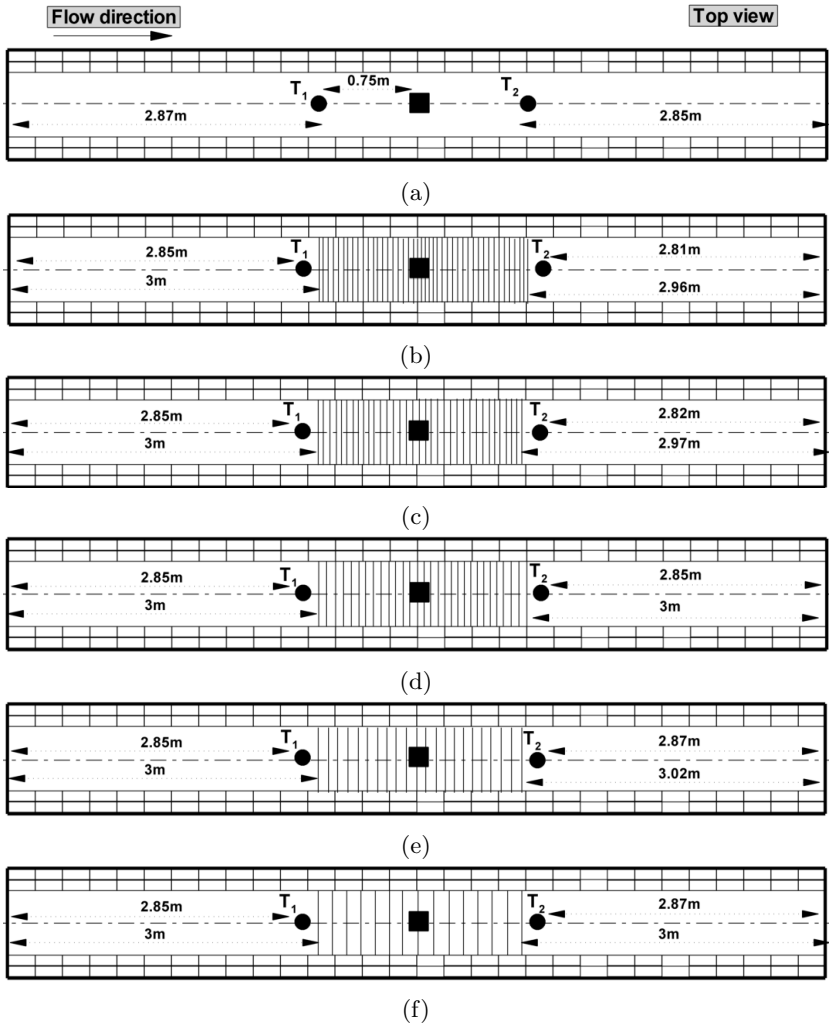

Figure 7.6 – Reference case (a) and bottom macro-roughness configurations $B1$ (b), $B1.5$ (c), $B2$ (d), $B3$ (e) and $B5$ (f) - ● and ■ symbols representing positions of turbidimeters T_1 and T_2 and water height measuring device, respectively

The direction of the flow is in the streamwise direction from left to right. To build the reference case, two rows of the limestone bricks are located longitudinally on each side of the experimental flume. The width of the channel is $0.6m$. The limestone bricks are aligned longitudinally in lateral roughness banks $L1$ and $L5$. They are positioned spanwisely in lateral roughness banks $L2$, $L3$ and $L4$. T_1 is the upstream turbidimeter and T_2 is the downstream one. Based on previous study [Maechler, 2016] of the SST in lateral macro-rough flows, it is supposed that up to $3m$ from the entrance, the flow could be perturbed and the deposition of sediment particles could be modified remarkably. Likewise,

the sediment concentration shown by the downstream turbidity could be biased up to $1m$ from the downstream regulating gate. For the reference case, the downstream probe T_2 is located $2.85m$ upstream of the exit gate and the upstream probe T_1 is positioned $2.87m$ downstream of the entrance. It circumvents totally perturbations from tranquilizing entrance structure and regulating exit gate. For the reference case, the deposition certainly takes place since there are many dead and trapping zones between bricks and walls and under regulating gates as well. Regarding lateral macro-rough cases, this necessary circumstance is not satisfied in some configurations in downstream or upstream parts. Maechler [2016] recorded that with the flow rate of 15 liter per second, free surface oscillations inside lateral cavities were detected. Also, there was a relationship between the amplitude of oscillating waves and sedimentation pattern and aspect ratio of lateral cavities. Here, to capture these oscillations of the free surface for lateral macro-rough flows, a camera is located inside the second cavity flow from the left side.
Figure (7.7a) shows the d-type bottom roughness in which $\vartheta = 1.0$. Figure (7.7b) manifests the k-type bottom roughness in which $\vartheta > 1.0$.

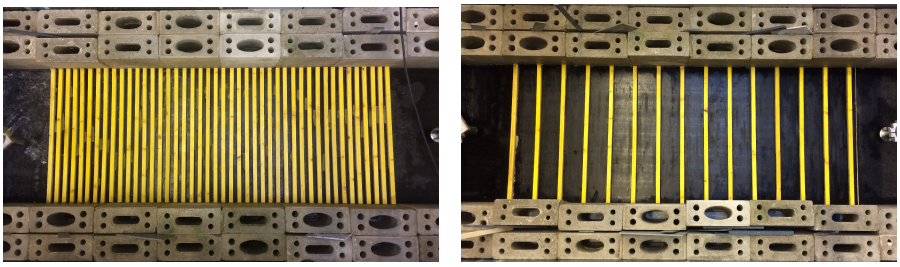

(a) (b)

Figure 7.7 – Bottom roughness: d-type ($\vartheta = 1.0$) (a) and k-type ($\vartheta = 5.0$) (b)

The distance between each turbidimeter, T_1 or T_2, and the last bottom roughness element in both sides is equal to $0.15m$. The number of bottom roughness elements and the length of the bottom rough area are shown in table (7.2). The water height measuring device shown by the square symbol is over the middle bar. Figure (7.8) manifests moment when both pumps are switched off and there is no water flowing in the open channel. Total volume of water inside the hydraulics system is equivalent to 3045 liter. In this study, because the concentration of suspended particles is generally lower than 3 gram per liter, the fluid is Newtonian. The imposed volumetric flow rate in all configurations is 15 liter per second under the steady state condition. It was mentioned by Maechler [2016] that the mean velocity took place at 40% of the flow depth from the bed. Accordingly, vertical positions of both turbidimeters, T_1 and T_2, are set $0.028m$ off the bed. In this experimental work, we select the frequency acquisition of $100Hz$ consequently 100 time steps are set in one second. The concentration of

the clear water in all configurations is less than 0.07 gram per liter at the beginning of the recording. For all configurations, $1.6kg$ of the Polyurethane particles is added to the clear water in the downstream tank exactly 5 minutes after the initiation of the recording on the LABVIEW. The total time of all experiments is 2 hours. The instantaneous concentration reduces more as the process proceeds more due to depositing sediments in the recirculating hydraulics system.

Table 7.2 – Number of bottom roughness elements and the length of the rough area

	$B1$	1.5	$B2$	$B3$	$B5$
Number of elements	44	35	29	22	15
Length of rough area	1.54m	1.53m	1.5m	1.48m	1.5m

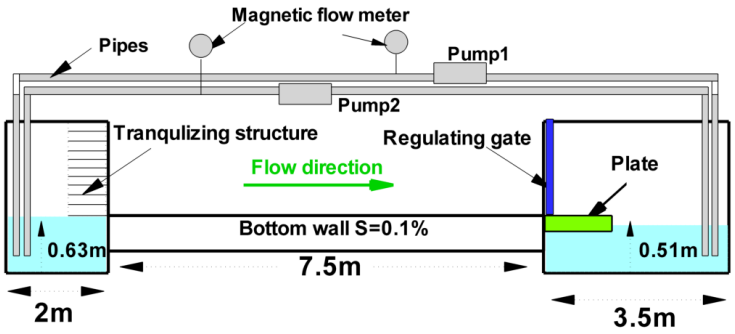

Figure 7.8 – Schematic of the hydraulics system

Table 7.3 – Relevant flow variables of the SLF in the reference case

Flow depth $h(m)$	0.07	Density ratio s	1.16
Aspect ratio AR	8.5	Particle diameter $d(m)$	0.00008
Hydraulic radius $R_h(m)$	0.0313	Settling velocity $w_s(\frac{m}{s})$	0.0005
Channel width (m)	0.6	Friction velocity $u_*(\frac{m}{s})$	0.0175
Volum. concentration C	0.00045	Particle Reynolds number Re_p	1.39
Discharge $Q(\frac{m^3}{s})$	0.015	Equivalent roughness $k_s(m)$	0.000089
Bulk velocity $\tilde{U}(\frac{m}{s})$	8.5	Mixture density $\rho_m(\frac{kg}{m^3})$	1000.072
Reynolds number Re	43773	Mixture viscosity $\nu_m(\frac{m^2}{s})$	0.000001
Froude number Fr	0.4268	Temperature $T(^{\cdot}C)$	20
Friction factor f	0.0192	Total time $t(s)$	7200

Table (7.3) displays pertinent flow variables for the sediment laden flow in the reference case. Each pump has a discharge of 7.5 liter per second. It is assumed that in the current flume with a aspect ratio of 8.5, there is no effect of the sidewalls on the velocity and sediment concentration. The settling velocity is obtained from equation (2.1) based on the particle diameter. The particle Reynolds number is less than 5.0, so the bed is hydraulically smooth according to experiments of Cellino [1998]. The equivalent roughness height is obtained from the well-known Colebrook and White equation. Based on the volumetric concentration, there is insignificant change in the kinematic viscosity and density. The friction velocity is approximated utilizing the energy-gradient procedure.

7.4 Experimental findings

In this study, the dependence of the deposition of Polyurethane particles on perturbations of the flow are confirmed by the video-recording. Some sedimentation patterns could be found in Maechler [2016]. The temporal auto-correlation $b(\theta)$ and cross-correlation $q(\theta)$ of sediment concentration signals C_1 and C_2 are calculated as,

$$b(\theta) = \frac{\overline{C'(t)C'(t+\theta)}}{\overline{C'^2(t)}} \tag{7.3}$$

$$q(\theta) = \frac{\overline{C_1'(t)C_2'(t+\theta)}}{\sqrt{\overline{C_1'^2(t)}}\sqrt{\overline{C_2'^2(t)}}} \tag{7.4}$$

θ is the time interval in second. The cross correlation provides a measure of how closely two signals of the sediment concentration measured with turbidimeters T_1 and T_2, are related. It is constructed as a scaled inner product of two functions integrated over a temporal domain of interest. In all reference and macro-rough flow cases, the imposed volumetric flow rate is identical and analysis is based on the steady flow condition. The flow is fully rough in the presence of bottom macro-rough elements.

7.4.1 Lateral macro-rough flow

Figure (7.9) shows a lateral cavity flow with pertinent variables. According to Juez et al. [2017], the aspect ratio ϑ_{cf} of the cavity flow, roughness aspect ratio RR and cavity density CD are,

$$\vartheta_{cf} = \frac{W_{cf}}{l_{cf}}, RR = \frac{W_{cf}}{L_{cf}}, CD = \frac{l_{cf}}{l_{cf} + L_{cf}} \tag{7.5}$$

From a flow pattern analysis point of view [Weitbrecht et al., 2008] [Akutina, 2015], when ϑ_{cf} is between 0.15 and 0.5, one large oval eddy is seen in cavity flows recirculating in the clockwise direction, while other one rotating in the counter-clockwise direction. Cavities with a large aspect ratio 0.8 demonstrate

a single circular eddy [Weitbrecht et al., 2008] [Akutina, 2015] rotating in the clockwise direction. It occupies nearly 80 percent of the length of the cavity flow and there is smallest length for eddies to develop.

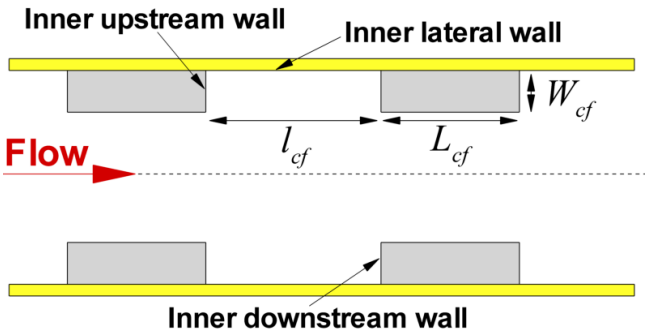

Figure 7.9 – Lateral cavity flow with pertinent variables

Because of the clockwise circulation of sediment particles, they mostly trap in a circular pattern in the middle of cavity flows. These were experimentally established in the literature using the particle tracking velocimetry (PTV) [Akutina, 2015] and particle image velocimetry (PIV) [Weitbrecht et al., 2008]. According to Meile [2007], for configurations $L1$ and $L5$ there is a low discharge. Ratio between the water depth $0.07m$ and the width of the narrow section of the channel $0.59m$ is lower than 0.12. For configurations $L2$, $L3$ and $L4$ there is a medium discharge. Ratio is between 0.12 and 0.3. With low discharge, the water surface is almost flat but tiny ripples may be developed at the free surface. On the other hand, with medium discharge, more waviness of the free surface is present and the cross-section area of the flow may be still homogeneous. Plus, longitudinal and transversal waves are present in the flume. Generally speaking, for lateral macro-rough cases, it is hard to depict the role of waves in filing and emptying of cavity flows.
Table (7.4) summarizes all germane variables and patterns for lateral macro-rough flows and reference case.

Table 7.4 – germane variables and patterns for lateral macro-rough flows

Configuration	ϑ_{cf}	RR	CD	Vortexes	Discharge
Reference	–	–	–	None	Low
$L1$	0.2	0.39	0.66	One big oval-One small	Low
$L2$	0.5	0.5	0.5	One big oval-One small	Medium
$L3$	0.5	0.62	0.55	One big oval-One small	Medium
$L4$	0.5	1.25	0.71	One big oval-One small	Medium
$L5$	0.8	0.39	0.33	Single circular eddy	Low

Figure (7.10) presents the temporal evolution of the normalized sediment con-

centration for the reference case and lateral macro-rough configurations. C_0 is the maximum of the sediment concentration for each configuration.

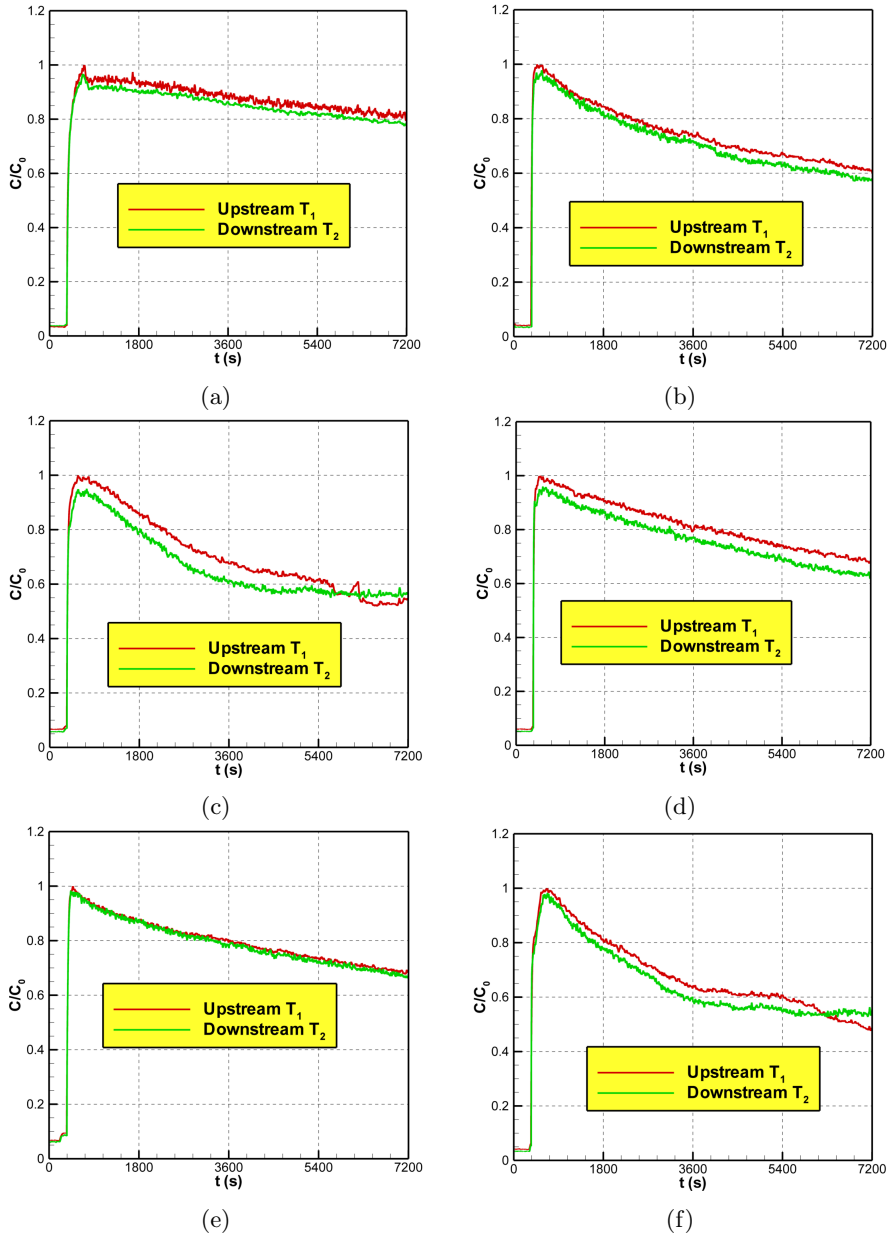

Figure 7.10 – Instantaneous normalized concentration for the reference (a) and lateral macro-rough configurations $L1$ (b), $L2$ (c), $L3$ (d), $L4$ (e) and $L5$ (f)

Figure (7.11) illustrates the temporal evolution of the auto-correlations $b(\theta)$ for the reference case and lateral macro-rough configurations.

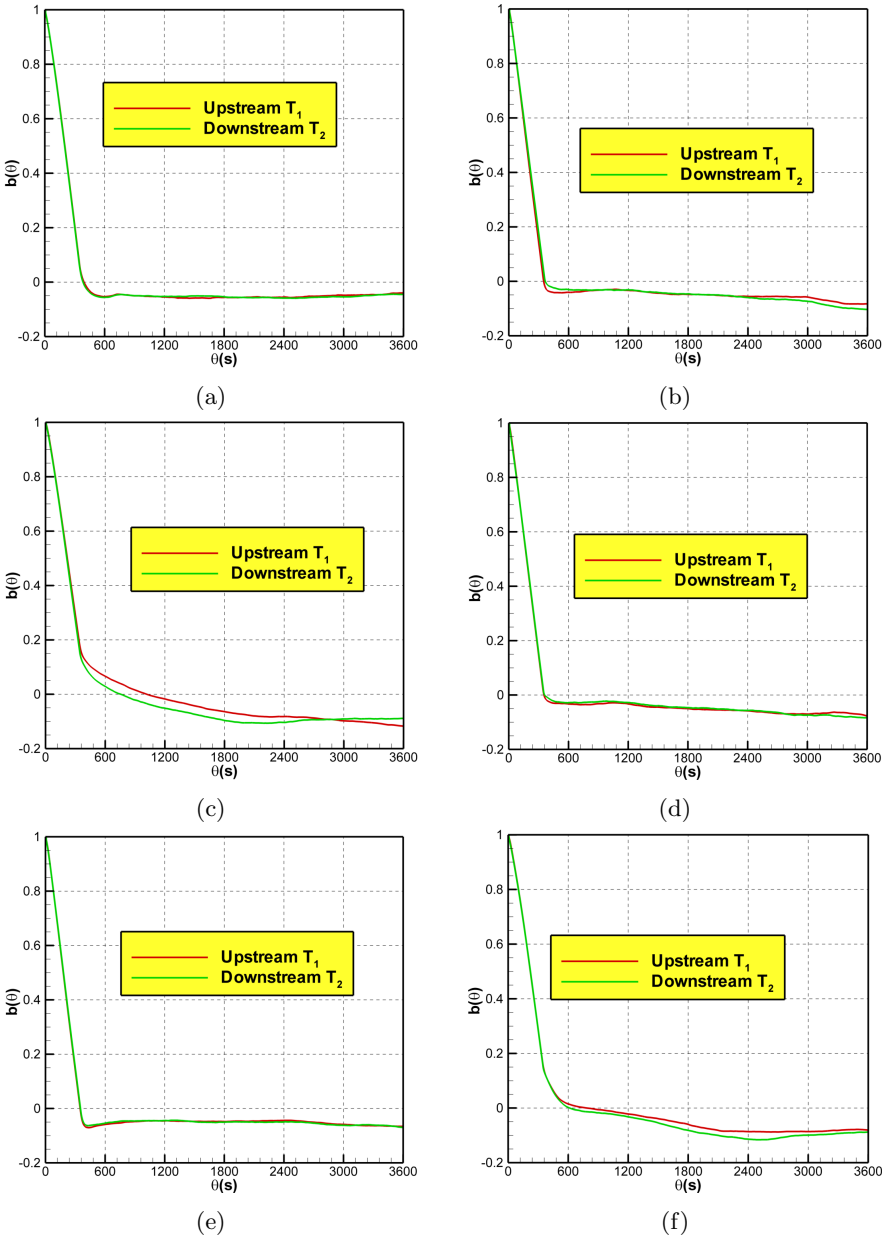

Figure 7.11 – Instantaneous auto-correlation for the reference (a) and lateral macro-rough configurations $L1$ (b), $L2$ (c), $L3$ (d), $L4$ (e) and $L5$ (f)

The decay of the time-dependent sediment concentration would not be identical from case to case. Regarding the upstream concentration signal C_1 , the corresponding decrease of the normalized sediment concentration over the two hour experiment for reference, $L1$, $L2$, $L3$, $L4$ and $L5$ configurations is approximately 0.2, 0.4, 0.45, 0.35, 0.3 and 0.5, respectively. Least decay of the normalized sediment concentration in the two hour experiment is seen for the reference case in absence of cavity flows. Sediment trapping and turbulence for lateral macro-rough flows depends on the lengths of inlet and outlet reach, flow discharge, aspect ratio ϑ_{cf} of the cavity flow, roughness aspect ratio RR and cavity density CD.

Juez et al. [2017] mentioned that lower sedimentation was for configurations with higher roughness RR and cavity density CD. Here, it is also seen that the least sedimentation or decrease of normalized sediment concentration among lateral configurations is for case $L4$ with highest $RR = 1.25$, $CD = 0.71$ and medium flow discharge.

Figure (7.10e) manifests that for case $L4$ there is almost no difference between instantaneous evolutions of normalized concentration signals C_1 and C_2. For case $L4$, the cavity aspect ratio is 0.5 and eddies, which are induced inside the cavity flow, are stretched into the main flow. Counter-rotating behavior of vortexes within the cavity flow generates mixing and removal of Polyurethane particles into the main flow. Length of the inlet reach for case $L4$ is $1.78m$ which is lowest amid other cases. It boosts the mixing of Polyurethane particles and turbulence in open channel flows. In contrast to other cases, the integral scale of concentration signals for case $L4$ is lower. It is understood from autocorrelations in figure (7.11e).

On the other hand, highest deposition of the Polyurethane particles is detected for case $L5$ with lowest $RR = 0.39$ and $CD = 0.33$. For case $L5$, the discharge is low and the Polyurethane particles accumulate in a circular pattern in the middle of the cavity flow. Comparing to the reference, $L1$, $L3$ and $L4$ cases, the turbulence is reduced for case $L5$. It could be observed from autocorrelations in figure (7.11f). Deposition of the Polyurethane particles for case $L2$ is also high. Figure (7.11c) demonstrates that the turbulence is most attenuated for case $L2$ with medium discharge in comparison with the reference, $L1$, $L3$, $L4$ and $L5$ cases. It is due to adequate lengths of the inlet and outlet reach. Consequently, the widening of the channel in case $L2$ is highly effective to deposit the Polyurethane particles in open channel flow.

The cross-correlations of two sediment concentration signals for the reference and lateral macro-rough configurations are depicted in figure (7.12). Cross-correlation demonstrates similarity between two turbulent signals of the sediment concentration. As would be detected, the cross-correlation of two turbulent signals of the sediment concentration for case $L2$ is high. It means that inserting configuration $L2$ induces similar signals since the widening of the channel in this configuration is highly effective in reducing the turbulence. Furthermore, cross-correlations for lateral cases $L1$, $L3$ and $L4$ are same but lower than that for the reference case. Cross-correlations for lateral cases $L2$, $L5$ are bigger than that for the reference case.

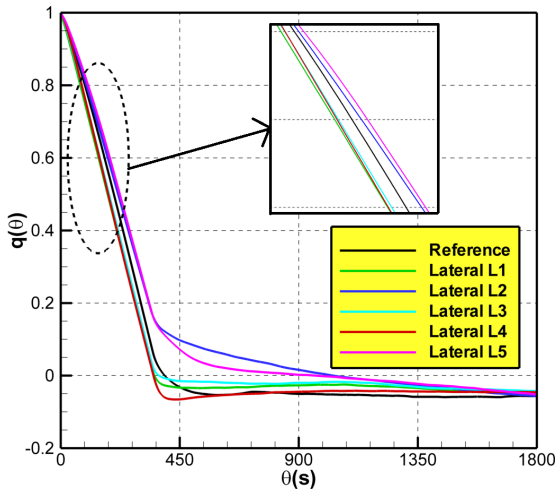

Figure 7.12 – Cross-correlations of two sediment concentration signals for the reference and lateral macro-rough configurations

7.4.2 Bottom macro-rough flow

Influences of spacing $1 \leq \vartheta \leq 5$ between bottom macro-rough elements on the instantaneous normalized sediment concentration and auto-correlation and cross-correlation of sediment concentration signals are discussed.
The instantaneous evolution of the normalized sediment concentration for the reference and bottom macro-rough configurations is presented in figure (7.13). C_0 is the maximum of the concentration of suspended Polyurethane particles detected in each configuration.
Figure (7.14) illustrates temporal auto-correlations of sediment concentration signals for the reference case and bottom macro-rough flows.
Regarding the downstream concentration signal C_2, corresponding reduction in the normalized sediment concentration over the two hour experiment for reference, $B1$, $B1.5$, $B2$, $B3$ and $B5$ configurations is approximately 0.2, 0.3, 0.3, 0.55, 0.3 and 0.3, respectively. For bottom macro-rough flows, the Polyurethane particles are trapped between bottom elements. As can be understood, bottom elements cause highest deposition and trapping of suspended Polyurethane particles in a specific spacing $\vartheta = 2$ ($B2$). Decrease in the normalized concentration signal C_2 is identical for all other bottom macro-rough flows. It is seen that difference between concentration signals C_1 and C_2, for cases $\vartheta = 1.0$ ($B1$) and $\vartheta = 1.5$ ($B1.5$) is lesser than that for the reference case. It can be said from auto-correlations that bottom elements lessen slightly the integral scale of turbulent signals of the concentration in cases $B1$ and $B1.5$ compared to the reference case. So, building cases $B1$ and $B1.5$ enhances a little mixing and turbulence in contrast to the reference case. According to autocorrelations, turbulence characteristics of C_1 and C_2 signals are similar for the reference, $B1$ and $B1.5$ cases. For spacing $\vartheta = 2$ ($B2$), the turbulence is most attenuated since

the integral scale of the downstream concentration signal C_2 in figure (7.14d) is biggest among other cases.

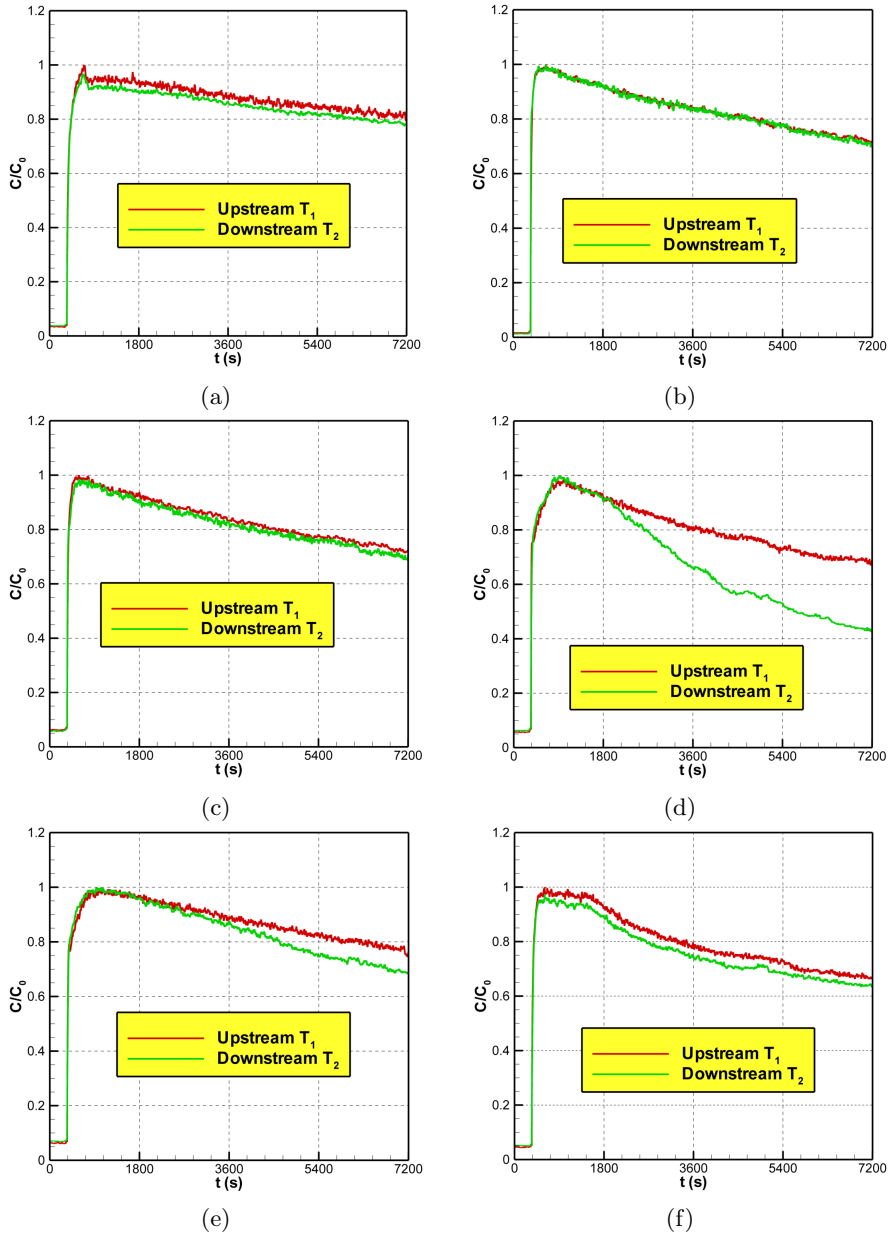

Figure 7.13 – Instantaneous normalized sediment concentration for the reference (a) and bottom macro-roughness configurations $B1$ (b), $B1.5$ (c), $B2$ (d), $B3$ (e) and $B5$ (f)

It engenders the highest difference between concentration signals C_1 and C_2 as process advances more. The trapping becomes less when the spacing increases from $\vartheta = 2.0$ to $\vartheta = 5.0$.

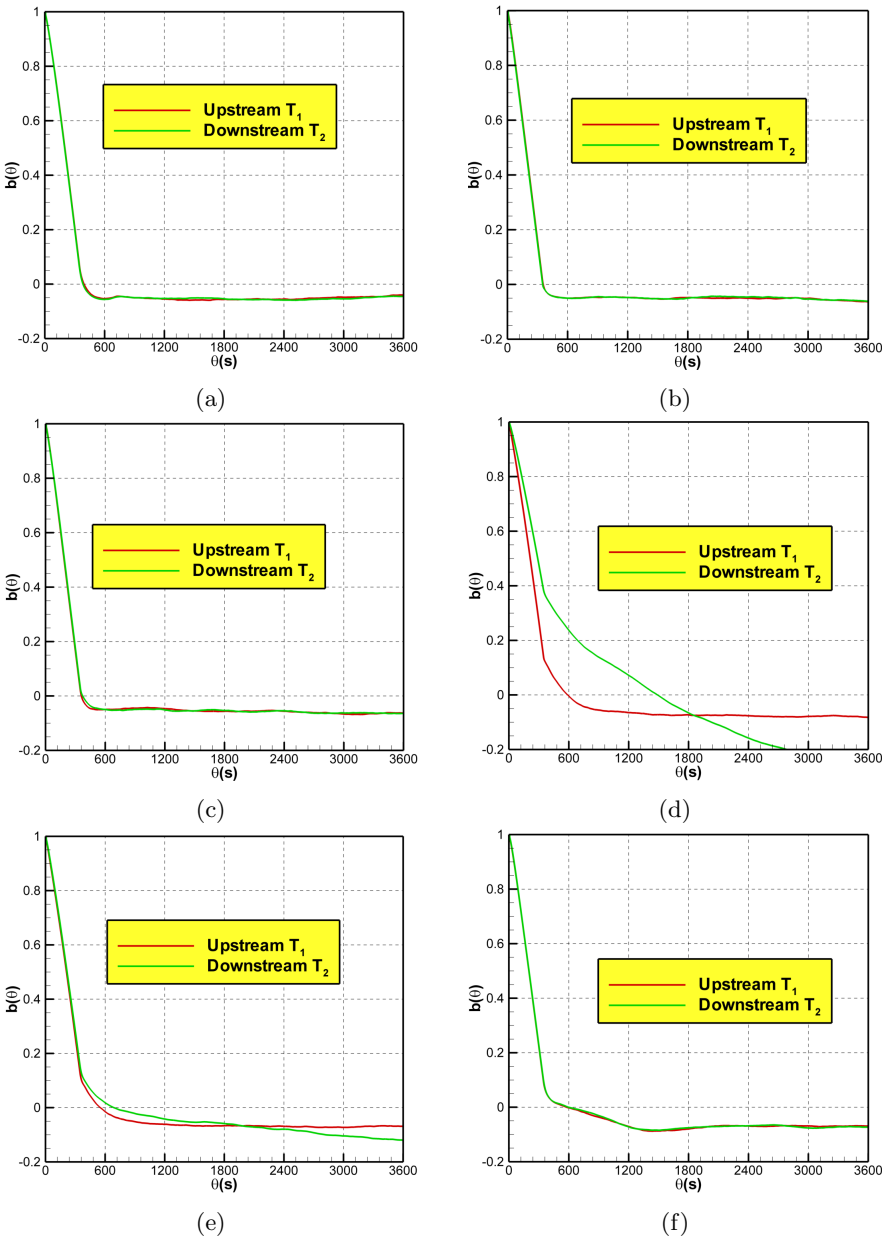

Figure 7.14 – Instantaneous auto-correlation for the reference (a) and bottom macro-roughness configurations $B1$ (b), $B1.5$ (c), $B2$ (d), $B3$ (e) and $B5$ (f)

This is in agreement with the increase of the turbulence or reduction of the integral scale of the downstream concentration signal C_2. It is seen from figures (7.14e) and (7.14f). As spacing is augmented from $\vartheta = 2$ $(B2)$ to $\vartheta = 5$ $(B5)$, auto-correlations computed from C_1 signal does not change anymore. Turbulence characteristics of C_1 and C_2 signals are similar for ratio $\vartheta = 5$ $(B5)$.
It could be stated that bottom macro-rough elements change significantly flow patterns and turbulence characteristics in a specific spacing ϑ. After that, as spacing gets larger, influences of bottom macro-roughness elements on each other in terms of flow patterns between elements diminish more. They start to be isolated elements.
In this study, the maximum effect of bottom macro-rough elements on concentration signals is observed for spacing $\vartheta = 2$ $(B2)$ instead of spacing $\vartheta = 7$ which reported earlier by Leonardi et al. [2003]. In examinations of Leonardi et al. [2003] and Leonardi et al. [2004], from a turbulence analysis viewpoint, there was no difference between ratios $\vartheta = 0.3, 0.6, 1, 2.07$. This discrepancy stems from fact that in their study, the turbulent Reynolds number Re_τ for the reference case was equal to 180 while in the present study, it is equivalent to 540. Therefore, the more turbulent Reynolds number increases in bottom macro-rough flows, the more sensitivity of turbulence structures to ϑ enhances.
Cross-correlations of two concentration signals for the reference and bottom macro-rough configurations are shown in figure (7.15). Cross-correlations for cases $B1$ and $B1.5$ are same but lower than that for the reference case. The maximum of the cross-correlation is seen for $B2$. Thus, highest attenuation of the turbulence induces most similar turbulent concentration signals. As we increase spacing from $\vartheta = 2$, the cross-correlation reduces.

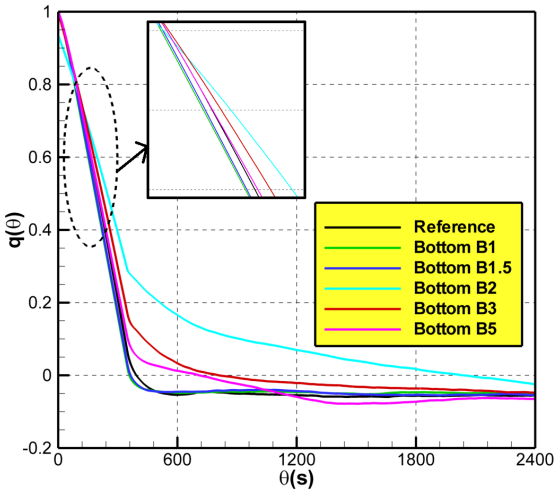

Figure 7.15 – Cross-correlations of two concentration signals for bottom macro-rough configurations and reference case

Chapter 8

Conclusions

SST in uniform turbulent open channel flows includes many complexities that complicate understanding of experimental data. Most of formulations developed for analyzing SST are based on the mixture perspective.
In this study, first of all, the single-phase Euler-Euler based wall-resolving LES with the dynamic Smagorinsky model in the LES-COAST code was implemented to understand interactions between suspended sand particles and turbulence in a turbulent open channel flow with high aspect ratio and bottom smooth wall. Fast-Eulerian method in the two-way coupling framework was used to explain effects of the sediment concentration on hydrodynamics of the mixture. Streamwise and vertical turbulence intensities for the clear water flow in experiment of Muste et al. [2005] were much bigger than those in the present wall-resolving LES and DNS by Hoyas and Jimenez [2008]. The bulk flow velocity in the sediment-laden flow was lesser than that in the clear water flow which illustrated that the suspension of sand particles resulted in the extraction of the energy from the flow. Moreover, the shear stress on the channel bed was same for both clear water and sediment-laden flows. Muste et al. [2005] from experimental point of view reported that the depth-averaged streamwise velocity of the mixture in inner region was higher than that of the clear water flow. There was strong particle flow turbulence and particle velocities were not affected by the no-slip condition. On other hand, in this study in the inner region it was seen that the depth-resolved streamwise velocity was not affected when sand particles were introduced into the clear water flow. In the outer region, the depth-resolved streamwise velocity was reduced.
Second of all, the single-phase Euler-Euler based unresolved wall-function LES with the Smagorinsky model under the equilibrium stress assumption in the LES-COAST code was employed to investigate the SST in a turbulent open channel flow with a low aspect ratio and a bottom rough wall. The reference concentration method proposed by Smith and Mclean [1977] together with the Shields diagram was used to treat the erosion of sediment particles from the channel bed. Wall shear stress on sidewalls must be considered in the com-

putation of the mixture flow in narrow open channels. When the modified gravity term, which was proposed by Dallali and Armenio [2015] in the Navier-Stokes equations of the mixture flow, was deactivated, the sediment concentration became large and unsatisfactory higher-order turbulence statistics for the sediment-laden flow were recorded. Hence, the buoyancy induced by suspended sand particles influenced remarkably hydrodynamics of the flow. Suspending sediment particles caused the reduction of the friction velocity, bulk velocity and roughness in contrast to the clear water flow. Streamwise velocity was decreased in the outer layer while it was enlarged in the super-saturated region near the channel bed. There were high inter-particle collisions between sediment particles which were not bounded by viscosity. Vertical velocities for the sediment-laden flow in lower levels were significantly higher than vertical velocities for the clear water flow. Close to free surface, vertical velocities for clear water and sediment-laden flows were equal. Streamwise turbulence intensity for the sediment-laden flow was bigger than that for the clear water flow except close to free surface where they were identical to experimental data of Cellino [1998]. Compared to the clear water flow, suspended sand particles generated slight enhancement of the vertical turbulence intensity near the channel bed while in upper levels, significant weakening of the vertical turbulence intensity occurred. Adjacent to the free surface, vertical turbulence intensities for clear water and sediment-laden flows were same since the sediment concentration was low.

It was concluded that systematic measurements and computations of the SST in turbulent open channel flows should be performed simultaneously. Experimental data could be used for the validation and development of the mixture flow model.

Third of all, impacts of lateral and bottom macro-rough boundaries on the propagation of a suspended sediment wave in a turbulent open channel flow were investigated experimentally under the steady state condition. In the reference case, there was no trapping and deposition zones, so there was the least decay of the normalized concentration of suspended Polyurethane particles. Least sedimentation amid lateral configurations was for case $L4$ with the highest roughness aspect ratio, cavity density and medium flow discharge. Cavity aspect ratio was 0.5 and counter-rotating vortexes inside the cavity flow removed Polyurethane particles into the main flow. Lowest length of the inlet reach was for case $L4$ which elevated mixing and turbulence. Autocorrelation showed that the integral scale of concentration signals for case $L4$ was lower than those for other cases. Highest deposition of the Polyurethane particles was for $L5$ case with the lowest roughness aspect ratio, cavity density and flow discharge. Polyurethane particles accumulated in a circular pattern in the middle of the cavity flow. Turbulence was most weakened for case $L2$ with the medium discharge due to adequate lengths of the inlet and outlet reach. Deposition of the Polyurethane particles was also high for case $L2$. From crosscorrelations it was found out that building case $L2$ engendered similar concentration signals since the turbulence was effectively abated. Consequently, the sediment trapping and turbulence in lateral macro-rough flows were related to the lengths of inlet and outlet reach,

flow discharge, aspect ratio of the cavity flow, roughness aspect ratio and cavity density. In the bottom macro-rough flows, the Polyurethane particles were trapped between bottom elements. According to autocorrelations, turbulence characteristics of C_1 and C_2 signals were identical for reference, $B1$ and $B1.5$ cases. When the spacing between bottom elements was $\vartheta = 2$ ($B2$), highest trapping of suspended Polyurethane particles occurred. Most weakening of turbulence and highest difference between concentration signals C_1 and C_2 was seen for spacing $\vartheta = 2$ ($B2$). As spacing was enhanced from $\vartheta = 2$ to $\vartheta = 5$, the integral scale of the downstream concentration signal C_2 was reduced, turbulence was enhanced and trapping became lesser. Crosscorrelations for cases $B1$ and $B1.5$ were identical but lesser than that for the reference case. Crosscorrelations established that most similar turbulent concentration signals took place for case $B2$ since the turbulence was highly attenuated. Bottom macro-rough elements altered significantly flow pattern and turbulence characteristics in a specific spacing ϑ. After that, as spacing got larger, the influence of bottom macro-roughness elements on each other abated more and they were isolated elements. The more turbulent Reynolds number was enhanced in flumes with bottom macro-rough elements, the more sensitivity of turbulence structures to ϑ was increased. It has prime importance for hydraulics engineers who artificially modify natural paths of rivers to do river restoration, sediment management and to control propagation of contaminants.

References

Y. Akutina. *Experimental investigation of flow structures in a shallow embayment using 3D-PTV*. PhD thesis, McGill University, 2015.

V. Armenio and U. Piomelli. Lagrangian mixed subgrid-scale model in generalized coordinates. *Flow, Turbul. Combust.*, 65:51–81, 2000.

V. Armenio and S. Sarkar. An investigation of stably stratified turbulent channel flow using large-eddy simulation. *J. Fluid Mech.*, 459:1–42, 2002.

A. Ashrafian and H.I. Andersson. The structure of turbulence in a rod-roughened channel. *Int. J. Heat Fluid Flow*, 27:65–79, 2006.

A. Ashrafian, H.I. Andersson, and M. Manhart. Dns of turbulent flow in a rod roughened channel. *Int. J. Heat Fluid Flow*, 25:373–383, 2004.

J. Bai, H. Fang, and T. Stoesser. Transport and deposition of fine sediment in open channels with different aspect ratios. *Earth Surf. Process. Landforms*, 38:591–600, 2013.

J.C. Bathurst. Flow resistance estimation in mountain rivers. *J. Hydraul. Engrg.*, 111:625–643, 1985.

S. Bisceglia, R.J. Smalley, R.A. Antonia, and L. Djenidi. Rough-wall turbulent boundary layers at relatively high reynolds number. In B. Dally, editor, *Proceedings of the 14th Australasian Fluid Mechanics Conference*. Adelaide University, 2001.

M. Breuer and M. Alletto. Efficient simulation of particle-laden turbulent flows with high mass loadings using LES. *Int. J. Heat Fluid Flow*, 35:2–12, 2012.

G.L. Brown and A. Roshko. On density effects and large structure in turbulent mixing layers. *J. Fluid Mech.*, 64:775–816, 1974.

Z. Cao, S. Egashira, and P.A. Carling. Role of suspended-sediment particle size in modifying velocity profiles in open channel flows. *Water Resour. Res.*, 39: 1–15, 2003.

M. Cellino. *Experimental study of suspension flow in open channels*. PhD thesis, École Polytechnique Fédérale de Lausanne (EPFL), 1998.

D.R. Chapman. Computational aerodynamics development and outlook. *AIAA J.*, 17 :1293–1313, 1979.

J. Chauchat and S. Guillou. On turbulence closures for twophase sediment-laden flow models. *J. Geophys. Res.*, 113 :C11017, 2008.

N.S. Cheng. Effect of concentration on settling velocity of sediment particles. *J. Hydraul. Engrg.*, 123 :728–731, 1997.

Z. Cheng and T.J. Hsu. A turbulence-resolving eulerian two-phase model for sediment transport. *Coast. Eng. Proc.*, 1 :74, 2014.

Z. Cheng, X. Yu, T.J. Hsu, and S. Balachandar. A numerical investigation of fine sediment resuspension in the wave boundary layeruncertainties in particle inertia and hindered settling. *Comput. Geosci.*, 83 :176–192, 2015.

F. Chiodi, P. Claudin, and B. Andreotti. A two-phase flow model of sediment transport : transition from bedload to suspended load. *J. Fluid Mech.*, 755 : 561–581, 2014.

Y.J. Chou and O.B. Fringer. Modeling dilute sediment suspension using large-eddy simulation with a dynamic mixed model. *Phys. Fluids*, 20 :115103, 2008.

N.L. Coleman. Velocity profiles with suspended sediment. *J. Hydraul. Res.*, 19 : 211–229, 1981.

J. Cui, V.C. Patel, and C.L. Lin. Large-eddy simulation of turbulent flow in a channel with rib roughness. *Int. J. Heat Fluid Flow*, 24 :372–388, 2003.

M. Dallali and V. Armenio. Large eddy simulation of two-way coupling sediment transport. *Adv. Water Resour.*, 81 :33–44, 2015.

J.W. Deardorff. A numerical study of three-dimensional turbulent channel flow at large reynolds numbers. *J. Fluid Mech.*, 41 :453–480, 1970.

S. Dey. *Fluvial Hydrodynamics : Hydrodynamic and Sediment Transport Phenomena*. Springer Berlin Heidelberg, 2014.

W.E. Dietrich. Settling velocity of natural particles. *Water Resour. Res.*, 18 : 1615–1626, 1982.

L. Djenidi, F. Anselmet, and R.A. Antonia. Lda measurements in a turbulent boundary layer over a d-type rough wall. *Exp. Fluids*, 16 :323329, 1994.

L. Djenidi, R. Elavarasan, and R.A. Antonia. The turbulent boundary layer over transverse square cavities. *J. Fluid Mech.*, 395 :271–294, 1999.

O.A. Druzhinin. On the two-way interaction in two-dimensional particle-laden flows : the accumulation of particles and flow modification. *J. Fluid Mech.*, 297 :49–76, 1995.

S. Elghobashi. On predicting particle-laden turbulent flows. *Appl. Sci. Res.*, 52 :309–329, 1994.

A. Fakhari. *Wall-Layer Modelling of massive separation in large eddy simulation of coastal flows*. PhD thesis, Universit degli studi di Trieste, 2015.

J. Ferry and E. Balachandar. A fast eulerian method for disperse two-phase flow. *Int. J. Multiphase Flow*, 27 :1199–1226, 2001.

N. Foroozani. *Numerical Study of Turbulent Rayleigh-Bnard Convection with Cubic Confinement*. PhD thesis, Universit degli studi di Trieste, 2015.

N. Foroozani, J.J. Niemela, V. Armenio, and K.R. Sreenivasan. Reorientations of the large-scale flow in turbulent convection in a cube. *Phys. Rev. E*, 95 : 033107, 2017.

A. Galea, M. Grifoll, F. Roman, M. Mestres, V. Armenio, A. Sanchez-Arcilla, and L. Zammit Mangion. Numerical simulation of water mixing and renewals in the barcelona harbour area : the winter season. *Environ. Fluid Mech.*, 14 : 1405–1425, 2014.

M. Germano, U. Piomelli, P. Moin, and W.H. Cabot. A dynamic subgrid-scale eddy viscosity model. *Phys. Fluids A*, 3 :1760–1765, 1991.

S. Ghosal and P. Moin. The basic equations for the large eddy simulation of turbulent flows in complex geometry. *J. Comput. Phys.*, 118 :24–37, 1995.

R.W. Gilbert, E.A. Zedler, S.T. Grilli, and R.L. Street. Progress on nonlinear-waveforced sediment transport simulation. *IEEE J. Oceanic Engrg.*, 32 : 236–248, 2007.

W.H. Graf and M. Cellino. Suspension flows in open channels : experimental study. *J. Hydraul. Res.*, 40 :435–447, 2002.

J. Guo and P.Y. Julien. Turbulent velocity profiles in sediment-laden flows. *J. Hydraul. Res.*, 39 :11–23, 2001.

J.C. Harris and S.T. Grilli. Large eddy simulation of sediment transport over rippled beds. *Nonlin. Processes Geophys. Discuss.*, 1 :755–801, 2014.

K. Horiuti. Assessment of two-equation models of turbulent passive-scalar diffusion in channel flow. *J. Fluid Mech.*, 238 :405–433, 1992.

S. Hoyas and J. Jimenez. Reynolds number effects on the reynolds-stress budgets in turbulent channels. *Phys. Fluid*, 20 :1–8, 2008.

J. Jimenez. Turbulent flows over rough walls. *Annu. Rev. Fluid Mech.*, 36 : 173196, 2004.

C. Juez, I. Buhlmann, G. Maechler, A.J. Schleiss, and M.J. Franca. Transport of suspended sediments under the influence of bank macro–roughness. *Earth Surface Processes Landforms*, 2017. doi : 10.1002/esp.4243.

K. Kawanisi and R. Shiozaki. Turbulent effects on the settling velocity of suspended sediment. *J. Hydraul. Engrg.*, 134 :261–266, 2008.

J. Kim, P. Moin, and R. Moser. Turbulence statistics in fully developed channel flow at low reynolds number. *J. Fluid Mech.*, 177 :133–166, 1987.

B. Kironoto. *Turbulence characteristics of non-uniform flow in rough open-channel*. PhD thesis, École Polytechnique Fédérale de Lausanne (EPFL), 1992.

S. Kundu and K. Ghoshal. Effects of secondary current and stratification on suspension concentration in an open channel flow. *Environ. Fluid Mech.*, 14 : 1357–1380, 2014.

F. Kyrousi, A. Leonardi, F. Zanello, and V. Armenio. Efficient coupling between a turbulent flow and mobile bed by means of the level-set method and immersed boundaries. In *The 26th International Ocean and Polar Engineering Conference*. International Society of Offshore and Polar Engineers, June-July 2016.

C. Le Ribault, S. Sarkar, and S.A. Stanley. Large eddy simulation of evolution of a passive scalar in plane jet. *AIAA J.*, 39 :1505–1516, 2001.

A. Leonard. Energy cascade in large eddy simulation of turbulent fluid flow. *Adv. Geophys.*, 18A :237–248, 1974.

S. Leonardi, P. Orlandi, R.J. Smalley, L. Djenidi, and R.A. Antonia. Direct numerical simulations of turbulent channel flow with transverse square bars on one wall. *J. Fluid Mech.*, 491 :229–238, 2003.

S. Leonardi, P. Orlandi, L. Djenidi, and R.A. Antonia. Structure of turbulent channel flow with square bars on one wall. *Int. J. Heat Fluid Flow*, 25 : 384–392, 2004.

S. Leonardi, P. Orlandi, and R.A. Antonia. Properties of d- and k-type roughness in a turbulent channel flow. *Phys. Fluid.*, 19 :125101, 2007.

W.K. Lewis, E.R. Gilliland, and W.C. Bauer. Characteristics of fluidized particles. *Ind. Engrg. Chem.*, 41 :1104–1114, 1949.

D.K. Lilly. Energy cascade in large eddy simulation of turbulent fluid flow. *Phys. Fluids*, A4 :633–635, 1992.

B. Lin and R.A. Falconer. Numerical modeling of threedimensional suspended sediment for estuarine and coastal waters. *J. Hydraul. Res.*, 34 :435–456, 1997.

V.Y. Lyapin. Hydraulic analysis of channels with increased artificial bottom roughness. *Hydrotech. Constr.*, 28 :290–293, 1994.

G. Maechler. Influence of bank macro-roughness on the transport of suspended sediments. Master's thesis, École Polytechnique Fédérale de Lausanne (EPFL), 2016.

M.R. Maxey. The gravitational settling of aerosol particles in homogeneous turbulence and random flow fields. *J. Fluid Mech.*, 174 :441–465, 1987.

A.J. Mehta. *An Introduction to Hydraulics of Fine Sediment Transport*. World Scientific Publishing Company, 2013.

T. Meile. *Influence of macro-roughness of walls on steady and unsteady flow in a channel*. PhD thesis, École Polytechnique Fédérale de Lausanne (EPFL), 2007.

T. Meile, J.L. Boillat, and A.J. Schleiss. Flow resistance caused by large-scale bank roughness in a channel. *J. Hydraul. Engrg.*, 137 :1588–1597, 2011.

M. Muste and V.C. Patel. Velocity profiles for particles and liquid in open-channel flow with suspended sediment. *J. Hydraul. Engrg.*, 123 :742–751, 1997.

M. Muste, K. Yu, I. Fujita, and R. Ettema. Two-phase versus mixed-flow perspective on suspended sediment transport in turbulent channel flows. *Water Resour. Res.*, 41 :1–22, 2005.

M. Muste, K. Yu, I. Fujita, and R. Ettema. Two-phase flow insights into open-channel flows with suspended particles of different densities. *Environ. Fluid Mech.*, 9 :161–186, 2009.

I. Nezu and R. Azuma. Turbulence characteristics and interaction between particles and fluid in particle-laden open channel flows. *J. Hydraul. Engrg.*, 130 :988–1001, 2004.

I. Nezu and H. Nakagawa. *Turbulence in Open-Channel Flows*. IAHR Monograph Series. A.A. Balkema, Rotterdam, 1993.

I. Nezu and W. Rodi. Open-channel flow measurements with a laser doppler anemometer. *J. Hydraul. Engrg.*, 112 :335–355, 1986.

K. Noguchi and I. Nezu. Particle–turbulence interaction and local particle concentration in sediment-laden open-channel flows. *J. Hydro-Environ. Res.*, 3 :54–68, 2009.

C.Y. Perng and R.L. Street. 3-d unsteady flow simulation : alternative strategies for a volume-average calculation. *Int. J. Numer. Methods Fluids*, 9 :341–362, 1989.

A.E. Perry, W.H. Schofield, and P.N. Joubert. Rough wall turbulent boundary layers. *J. Fluid Mech.*, 37 :383–413, 1969.

A. Petronio, F. Roman, C. Nasello, and V. Armenio. Large eddy simulation model for wind-driven sea circulation in coastal areas. *Nonlin. Processes Geophys.*, 20 :1095–1112, 2013.

U. Piomelli. Wall-layer models for large-eddy simulations. *Prog. Aerosp. Sci.*, 44 :437–446, 2008.

U. Piomelli and E. Balaras. Wall-layer models for large-eddy simulations. *Annu. Rev. Fluid Mech.*, 34 :349–374, 2002.

M.B. Pittaluga. Stratification effects on flow and bed topography in straight and curved erodible streams. *J. Geophy. Res.*, 116 :F03026, 2011.

S.B. Pope. *Turbulent flows*. Cambridge University Press, 2000.

M. Righetti and G.P. Romano. Particle-fluid interactions in a plane nearwall turbulent flows. *J. Fluid Mech.*, 505 :93–121, 2004.

F. Roman, G. Stipcich, V. Armenio, R. Inghilesi, and S. Corsini. Large eddy simulation of mixing in coastal areas. *Int. J. Heat Fluid Flow*, 31 :327–341, 2010.

H. Romdhane, A. Soualmia, L. Cassan, and L. Masbernat. Evolution of flow velocities in a rectangular channel with homogeneous bed roughness. *Int. J. Engrg. Res.*, 6 :120–125, 2017.

U. Schumann. Subgrid-scale model for finite difference simulation of turbulent flows in plane channels and annuli. *J. Comput. Phys.*, 18 :376–404, 1975.

H. Shamloo and B. Pirzadeh. Analysis of roughness density and flow submergence effects on turbulence flow characteristics in open channels using a large eddy simulation. *Appl. Math. Model.*, 39 :1074–1086, 2015.

J. Smagorinsky. General circulation experiments with the primitive equations. *Mon. Weather Rev.*, 91 :99–165, 1963.

J. Smith and S. Mclean. Spatially averaged flow over a wavy surface. *J. Geophys. Res.*, 82 :1735–1746, 1977.

A. Soldati and C. Marchioli. Sediment transport in steady turbulent boundary layers : Potentials, limitations, and perspectives for lagrangian tracking in DNS and LES. *Adv. Water Resour.*, 48 :18–30, 2012.

M.F. Tachie, D.J. Bergstrom, and R. Balachandar. Rough wall turbulent boundary layers in shallow open channel flow. *J. Fluid. Engrg.*, 122 :533–541, 2000.

H. Tennekes and J.L. Lumley. *A First Course in Turbulence*. MIT Press, Cambridge, Mass., 1972.

E.A. Toorman. Validation of macroscopic modeling of particle-laden turbulent flows. In E. Dick, J. Vierendeels, F. Cantrijn, G. Campion, and C. Lacor, editors, *Proceedings 6rd Belgian National Congress on Theoretical and Applied Mechanics*. Ghent University, May 2003.

L.C. van Rijn. Sediment transport, part I : bed load transport. *J. Hydraul. Engrg.*, 110 :1431–1455, 1984a.

L.C. van Rijn. Sediment transport, part II : suspended load transport. *J. Hydraul. Engrg.*, 11 :1613–1641, 1984b.

V.A. Vanoni. *Sedimentation Engineering*. ASCE Manuals and Reports on Engineering Practices, 1975.

C. Villaret and A.G. Davies. Modelling sediment-turbulent flow interactions. *Appl. Mech. Rev., ASME*, 48 :601–609, 1995.

X. Wang and N. Qian. Turbulence characteristics of sediment-laden flow. *J. Hydraul. Engrg.*, 6 :781–800, 1989.

V. Weitbrecht, S.A. Socolofsky, and G.H. Jirka. Experiments on mass exchange between groin fields and the main stream in rivers. *J. Hydraul. Engrg.*, 134 : 173–183, 2008.

J.C. Winterwerp. Stratification effects by cohesive and noncohesive sediment. *J. Geophys. Res.*, 106 :22559–22574, 2001.

W. Wu, W. Rodi, and T. Wenka. Role of suspended-sediment particle size in modifying velocity profiles in open channel flows. *J. Hydraul. Engrg.*, 126 : 4–15, 2000.

J. Yan, H. Tang, Y. Xia, K. Li, and Z. Tian. Experimental study on influence of boundary on location of maximum velocity in open channel flows. *Water Sci. Engrg.*, 4 :185–191, 2011.

S. Yang, S. Tan, and X. Wang. Mechanism of secondary currents in open channel flows. *J. Geophys. Res.*, 117 :1–13, 2012.

S.Q. Yang, S.K. Tan, and S.Y. Lim. Velocity distribution and dip phenomenon in smooth uniform open channel flows. *J. Hydraul. Engrg.*, 130 :1179–1186, 2004.

K. Yu, B. Yoon, and D. Kim. Re-evaluation of change of mean velocity profiles in turbulent open-channel flows due to introducing sediment particles. *KSCE J. Civil Engrg.*, 18 :2261–2267, 2014.

Y. Zang, R.L. Street, and J.R. Koseff. A non-staggered grid, fractional step method for time-dependent incompressible navierstokes equations in curvilinear coordinates. *J. Comput. Phys.*, 114 :18–33, 1994.

G. Zanier, A. Petronio, and V. Armenio. The effect of coriolis force on oil slick transport and spreading at sea. *J. Hydraul. Res.*, 55 :409–422, 2017.

E.A. Zedler and R.L. Street. Large-eddy simulation of sediment transport : currents over ripples. *J. Hydraul. Engrg.*, 127 :444–452, 2001.

E.A. Zedler and R.L. Street. Sediment transport over ripples in oscillatory flow. *J. Hydraul. Engrg.*, 132 :180–193, 2006.

H. Zhu, L.L. Wang, and H.W. Tang. Large-eddy simulation of suspended sediment transport in turbulent channel flow. *J. Hydrodyn. Ser. B*, 25 :48–55, 2013.

Publications

[1] M. Jourabian, V. Armenio. **Large eddy simulation (LES) of suspended sediment transport (SST) at a laboratory scale**, The 26th International Ocean and Polar Engineering Conference, Rhodes, Greece, 26 June-2 July 2016.

[2] M. Jourabian, V. Armenio. **Wall-layer model for large eddy simulation (LES) of suspended sediment transport (SST) in a lab-scale turbulent open channel flow**, 13th International Conference on Heat Transfer, Fluid Mechanics and Thermodynamics (HEFAT2017), Portoroz, Slovenia, 17-19 July 2017.